Word count: 8408 (including references)

Revision 1

Trace element fractionation in magnetite as a function of Fe depletion from ore fluids at the Baijian Fe-(Co) skarn deposit, eastern China: Implications for Co mineralization in Fe skarns

Guang Wen[1,2], Jian-Wei Li[1,2*], Albert H. Hofstra[3], Daniel E. Harlov[2,5,6], Xin-Fu Zhao[1,2], Heather A. Lowers[3], Alan E. Koenig[4]

[1] *State Key Laboratory of Geological Processes and Mineral Resources, China University of Geosciences, Wuhan 430074, China*

[2]*2School of Earth Resources, China University of Geosciences, Wuhan 430074, China*

[3]*U.S. Geological Survey, DFC, MS-963, P.O. Box 25046, Denver, Colorado 80225*

[4] *Newmont, Technical Services, 10101 East Dry Creek Road, Englewood, Colorado, USA, 80112*

[5]*Deutsches GeoForschungsZentrum – GFZ, Telegrafenberg, 14473 Potsdam, Germany*

[6]*Department of Geology, University of Johannesburg P.O. Box 524, Auckland Park, 2006 South Africa*

* *E-mail: jwli@cug.edu.cn*

ABSTRACT

Magnetite is common in various magmatic and hydrothermal ore deposit types, and its trace element geochemistry has become increasingly used in ore genesis studies and mineral exploration. While fractional crystallization has been shown to influence the chemistry of igneous magnetite, the extent to which this process regulates the trace element composition of hydrothermal magnetite remains poorly understood. In this study, we analyzed trace elements in hydrothermal magnetite from the Baijian Fe-(Co) skarn deposit in eastern China and used Rayleigh and equilibrium fractionation modeling to demonstrate the importance of magnetite precipitation in controlling fluid and magnetite chemistry during Fe skarn mineralization.

The Baijian Fe-(Co) skarn deposit has 3 stages of magnetite. From early Mag-1 to later Mag-2 and Mag-3, the concentrations of compatible elements (Ni and V) decrease, whereas those of incompatible elements (Zn, Mn and Co) increase. There are obvious trends of increasing incompatible/compatible element ratios (e.g., Co/Ni, Zn/V, and Zn/Ni) and decreasing compatible/incompatible element ratios (e.g., V/Mn, Ni/Mn, and V/Co) from Mag-1 to Mag-3, with strong correlations between each of these ratios. Such systematic trace element variations in successive stages of magnetite can be best explained by increasing degrees of fractional crystallization with time. The wide range of incompatible/compatible element ratios (spanning 2-4 orders of magnitude) in Mag-2 and Mag-3 suggests that magnetite crystallization follows a process akin to Rayleigh fractionation.

Results from this study highlight the significant role that magnetite

crystallization during skarn formation has on the trace element chemistry of this mineral. Moreover, as the crystallization of magnetite progresses, the Co/Fe ratio of residual hydrothermal fluids is elevated, which favors the precipitation of Co in late-stage sulfides. This process helps to explain why some Fe skarn deposits as well as magnetite-rich IOA and IOCG deposits are potentially important economic sources for Co, currently necessary as one component in Li-ion batteries.

Key words: Magnetite geochemistry; Rayleigh fractionation; Cobalt mineralization; Iron skarn

INTRODUCTION

Magnetite is a common accessory mineral in a wide range of rocks and is a major mineral phase in a variety of hydrothermal ore deposit types, such as Fe skarns, Kiruna type iron oxide-apatite (IOA) deposits, and iron oxide-copper-gold (IOCG) deposits (Nadoll et al., 2014; Dare et al., 2014; Hu et al., 2014; Huang et al., 2018; Reich et al., 2022; Zhang et al., 2023). Magnetite has an inverse spinel structure and can accommodate a range of trace elements into its structure. It is resistant to mechanical breakdown and low temperature weathering/alteration, thus making it a powerful tool in igneous petrology and provenance studies (Grigsby, 1990; Lindsley, 1991; Dare et al., 2014; Canil and Lacourse, 2020; Luo et al., 2022). Recent studies have demonstrated the utility of magnetite trace element geochemistry as an important indicator for ore genesis studies and mineral exploration (Dupuis and Beaudoin, 2011; Nadoll et al., 2012; Dare et al., 2015; Knipping et al., 2015; Duparc et al., 2016; Canil et al., 2016; Pisiak et al., 2017; Ward et al., 2018; Huang and Beaudoin, 2019; Song et al., 2021; Zeng et al., 2022; Zhang et al., 2020).

The melt/fluid composition has been considered as the primary control on magnetite chemistry. In igneous systems, the melt composition can be significantly modified by the process of fractional crystallization (Gast, 1968). This process allows the residual melt, and thus magnetite crystallizing from it, to be depleted in compatible elements and enriched in incompatible elements. For example, Dare et al. (2014) found that compatible elements (Mg, Ni, Co, V, and Cr) in magnetite gradually decrease while incompatible elements (Ga, Ge, Hf, Mn, Mo, Nb, Sc, Sn, Ta, Ti, W, Zn,

and Zr) increase going from the lower to upper zones of the layered intrusions, such as the Bushveld Complex and Sept Iles. They interpreted this variation trend in terms of fractional crystallization of olivine, pyroxene, and magnetite. To date, however, few studies have investigated the effect of fractional crystallization on the composition of magnetite in hydrothermal regimes, and it remains unclear whether progressive precipitation of magnetite has a significant effect on fluid and mineral chemistry in hydrothermal magnetite deposits, such as Fe skarn, IOA, and IOCG deposits.

Iron skarns are among the largest skarn deposits in the world, with many containing >1 billion tons of ore (Meinert et al. 2005 and references therein). Iron skarns often contain significant quantities of Co, a technologically important metal in high demand, which occurs as a co-product or by-product (Einaudi et al., 1981; Rose et al., 1985; Meinert et al. 2005; Slack et al., 2017; Zhao et al., 2019; Wei et al., 2021; Yan et al., 2021; Shi et al., 2023). Magnetite is the predominant ore mineral in Fe skarns, while sulfides, although minor, serve as the primary host for Co in these deposits (Slack et al., 2017; Zhao et al., 2019; Wei et al., 2021; Yan et al., 2021; Shi et al., 2023). In this study, we analyze the trace element composition of magnetite from the Baijian Fe-(Co) skarn deposit in the North China Craton (NCC). Building upon recent experimental findings on magnetite-fluid trace element partitioning (Tauson et al., 2015, 2017; Smagunov et al., 2021), we perform Rayleigh and equilibrium fractionation modeling in order to illustrate how progressive magnetite precipitation influences both the fluid and magnetite chemistry during formation of an Fe skarn

97 deposit. Furthermore, we discuss the key role that magnetite precipitation has on Co
98 enrichment in late-stage sulfides.
99
100 # GEOLOGICAL BACKGROUND
101 ## Regional geology
102 The Baijian Fe skarn deposit is located in the northeastern part of the
103 Handan-Xingtai district in the central NCC. It is bounded to the north by southern
104 margin of the Central Asian Orogenic Belt and to the south by the Dabie-Sulu
105 ultra-high pressure belt (Fig. 1). The NCC was formed and subsequently stabilized at
106 ca. 1.85 Ga following the collision between the Western and Eastern Blocks along the
107 Trans-North China Orogen (Zhao et al., 2005). The Handan-Xingtai district is
108 characterized by unmetamorphosed Paleozoic marine sedimentary rocks of ~3,500 m
109 thickness that are underlain by the Precambrian crystalline basement (Fig. 1). The
110 Cambrian strata consist of limestones, sandstones, and shales, which are conformably
111 overlain by early Ordovician dolomites. Middle Ordovician strata conformably overly
112 the early Ordovician dolomites and consist chiefly of evaporite-bearing carbonates.
113 Carboniferous and Permian shales, mudstones, siltstones, sandstones and coal beds,
114 with a total thickness of 1,300 to 1,600 m, unconformably overlie the Ordovician
115 sequences and are mainly exposed in the eastern part of the district.
116 The Paleozoic sedimentary rocks are intruded by several major plutons and
117 associated numerous smaller stocks and dikes, which are dominated by diorite,
118 monzodiorite or syenite (Fig. 1). The Handan-Xingtai district hosts more than 100 Fe

skarn deposits that combined have total Fe reserves over 900 million tons (Mt). Those deposits are hosted in the diorite and monzodiorite intrusions, along the contact zones between the intrusions and surrounding carbonate sequences, or within fracture zones of the carbonate proximal to the intrusions. Zircon U-Pb geochronological studies have shown that the district-wide intrusions are early Cretaceous in age that were emplaced in the interval of 136 ± 2 to 128.9 ± 0.9 Ma (Sun et al., 2014; Deng et al., 2015; Sun et al., 2019a). Geochemistry and Sr-Nd-Hf isotope data indicate that they formed as a result of mixing between crustal-derived and enriched mantle-derived magmas, which originated during the thinning and destruction of mantle lithosphere beneath the NCC. This process was ultimately triggered by subduction of the paleo-Pacific plate underneath the eastern China continental margin (Chen et al., 2004; Chen et al., 2008; Shen et al., 2013).

Deposit geology

The Baijian Fe-(Co) skarn deposit has proven reserves of 112 million tons (Mt) ore at an average grade of 47.6 % Fe and contains 17,186 t Co as by product (Zhao, 2013). Drill cores reveal the ore hosting sedimentary rocks at Baijian Fe skarn are the middle Ordovician Majiagou Formation and Cixian Formation (Fig. 2), which mainly consist of dolomitic limestone and limestone with interlayered evaporites. The deposit is related to a fine grained, pinkish-gray, monzodiorite stock, which consists of amphibole, plagioclase, K-feldspar, and quartz, with minor to trace amounts of magnetite, titanite, fluorapatite, and zircon. The monzodiorite stock has experienced

141 extensive albitization. The most intensely albitized rocks consist of albite (70–80
142 vol.%), amphibole, plagioclase, K-feldspar, epidote, pyroxene, calcite, and titanite,
143 along with minor magnetite and fluorapatite. A diorite porphyry intrudes the Fengfeng
144 Formation but is not associated with hydrothermal alteration or mineralization.

145 The Baijian skarn deposit consists of two major Fe bodies (No.1 and No.2) that
146 developed at or proximal to the contact zone between the monzodiorite intrusion and
147 dolomitic limestone of the Middle Ordovician Majiagou Formation (Fig. 2). Both
148 orebodies strike northwest and have flat lenticular to stratiform morphologies. No.1
149 ore body is 1,450 m long and, 500 m wide, and ranges from a few to 138 m thick. It
150 occurs 450 to 1000 m below the present ground surface. The ore body extends
151 upwards from the monzodiorite contact into the dolomitic limestones of the Majiagou
152 and Cixian Formations (Fig. 2). No.2 ore body is 1,200m long, 600 m wide, has an
153 average thickness of 9 m and occurs at a depth of 580 to 750 m below the surface.
154 The ore body follows the contact between the monzodiorite and dolomitic limestones
155 of the Majiagou Formation.

156 Skarns are variably developed in the contact zones. Endoskarn mostly occurs as
157 irregular veins within the albitized, monzodiorite stock. The endoskarn veins are
158 typically a few centimeters wide, consisting chiefly of pyroxene with minor amounts
159 of fluorapatite, albite, and calcite. The pyroxene in the endoskarn belongs to diopside
160 (Di)-hedenbergite (Hd) series, ranging in composition from $Di_{89}Hd_{11}$ to $Di_{70}Hd_{30}$
161 (Wen et al., 2020). Exoskarn is massive in the lower part of the contact zone (Fig. 2),
162 which consists of an early prograde and a late retrograde assemblage. The prograde

skarn assemblages are dominated by pyroxene (Figs. 3A) with minor olivine, titanite, and fluorapatite. Pyroxene in the exoskarn is diopside-rich ($Di_{75-97}Hd_{3-24}$) (Wen et al., 2020). The retrograde skarn assemblages are composed of tremolite, phlogopite, and serpentine that commonly overprint or replace the prograde skarn minerals. Magnetite is the predominant ore mineral (Figs. 3B-F). It is disseminated through the exoskarn close to the intrusive contact and as massive bodies close to enclosing marble. Sulfides mainly occur in the upper part of ore bodies in the vicinity of marble. The sulfides are dominated by pyrite locally associated with traces of chalcopyrite and sphalerite. They are disseminated through the magnetite ores (Figs. 3E and F). Drill core logs reveal a general zonation pattern from massive pyroxene skarn close to the intrusive contract, followed by a magnetite-tremolite-phlogopite assemblage in the middle, and a distal magnetite-pyrite-calcite-serpentine assemblage close to marble.

SAMPLES AND METHODS

Three samples of massive pyroxene skarn and 21 samples of magnetite ore were collected for this study. Polished sections were examined using a petrographic microscope and SEM at the United States Geological Survey (USGS) in Denver. The massive pyroxene skarn samples are dominated by diopsidic pyroxene (> 90 vol.%) with minor disseminated magnetite (Fig. 3A). The magnetite ore samples can be categorized into two types based on their mineral assemblages: (1) magnetite ore associated with the retrograde skarn assemblage (n=11) and (2) magnetite ore associated with sulfides (n=10). Ore samples from the retrograde skarn contain 60 to

185 90 vol.% magnetite, and various amounts of tremolite, phlogopite, and serpentine;
186 sulfides are absent (Figs. 3B-D). Ore samples containing sulfides consist of massive
187 magnetite (>vol. 70%) with small amounts of pyrite and calcite that occur as
188 disseminations or in veinlets; retrograde minerals are absent or present locally (Fig.
189 3E-F).

190 Trace element concentrations in magnetite were determined by laser ablation
191 inductively coupled plasma-mass spectrometry (LA-ICP-MS) at the USGS (Denver).
192 Analyses were conducted using a Photon Machines Analyte G2 LA system (193 nm, 4
193 ns excimer) attached to a Perkin Elmer DRC-e ICP-MS. Depending on the size of the
194 magnetite grains targeted, ablation was carried out using a spot size of 40 or 65
195 micrometers at 8 J/cm^2. Single spot analyses were ablated using 10 and 13 pulses/sec
196 (10 and 13 Hz). Ablated materials were transported via a He carrier gas to a modified
197 glass mixing bulb where He and sample were mixed coaxially with Ar prior to the ICP
198 torch. Concentration calculations were conducted using the protocol of Longerich et
199 al. (1997). Signals were calibrated using USGS GS-series basaltic glasses GSD-1g
200 and GSE-1g (Nadoll and Koenig, 2011). Reference materials were analysed 5 to 10
201 times at the beginning of each analytical session and monitored throughout the session
202 for drift. Signals were screened visually for heterogeneities such as micro-inclusions
203 or zoning. The Fe content of an ideal stoichiometric magnetite was used as the
204 internal standard (Dare et al., 2012).

205 Additionally, five least-altered samples were collected from the Baijian
206 monzodiorite for major elements and cobalt concentration analysis. Samples were

cleaned with deionized water, subsequently crushed and powdered in an agate mill. Both major elements and cobalt concentration analysis were conducted at the ALS Mineral (Guangzhou) Co. Ltd, Guangzhou, China. The major oxides were measured by an X-ray fluorescence (XRF) spectrometer. The lithium borate fusion method was used and the relative standard deviations are better than 5%. Whole-rock cobalt concentrations were analyzed by ICP-MS with an Agilent 7900. For each sample, 50 mg of sample powder (200 mesh) was digested in Teflon bombs with perchloric, nitric and hydrofluoric acids. The residue was leached with dilute hydrochloric acid and diluted to volume. It was then analyzed by ICP-MS. Results were corrected for spectral inter-element interferences.

RESULTS

Magnetite petrography

Three types of magnetite were identified in this study based on their distribution in the drill core logs and textural relationships with other minerals observed in polished thin sections. Type 1 (Mag-1) is found in massive pyroxene skarn (Fig. 3A) and occurs as inclusions within, or in interstices between, the pyroxene crystals (Fig. 4A-B). It is subhedral, ranging in diameter from 200 μm to 1 mm and commonly contains mineral inclusions mainly of fluorapatite and pyroxene (Fig. 4C). The aforementioned textural relationships indicate broadly coeval formation of magnetite and pyroxene. Type 2 magnetite (Mag-2) occurs in the magnetite ore associated with the retrograde skarn assemblage (Fig. 3B-D). It is subhedral to euhedral, ranges in diameter from 500 μm to 1 cm. It is intergrown with retrograde minerals such as

tremolite, phlogopite, and serpentine, which locally replace prograde pyroxene and olivine (Fig. 4D-I). Type 3 magnetite (Mag-3) occurs in magnetite ore associated with sulfides (Fig. 3E-F). It is subhedral to euhedral, 500 μm to 5 mm in size, and coexists with pyrite and calcite (Fig. 4J). Some Mag-3 grains are replaced by hematite, calcite, and siderite (Fig. 4K-L). The textural relations suggest that overall, Mag-1 predates Mag-2 that formed earlier than Mag-3.

Trace element compositions of magnetite

Results from LA-ICP-MS spot analysis of magnetite (n = 257) are listed in appendix table A1 and are displayed on Figure 5. Most of the spots analysed revealed variable concentration in Mg, Al, Ti, V, Cr, Mn, Co, Ni, Zn, and Ga. Mag-1 has high concentrations of Ti, V, Ni, Cr, and Ga and relatively low concentrations of Mg, Mn, and Zn (Fig. 5). Mag-2 contains significantly lower concentrations of Ti, V, Ni, Cr, and Ga but higher concentrations of Mg, Mn and Zn (Fig. 5). Mag-3 has the lowest concentration of Ti, V, Ni, Cr and Ga but the highest concentration of Mg, Mn, and Zn. Cobalt is enriched in Mag-2 relative to Mag-1 and Mag-3 (Fig. 5). Compared with the other two equivalents, Mag-3 has a wider range of Co contents (Fig. 5). The Zn/Ni ratios are positively correlated with Zn/V and Co/Ni ratios, whereas the reverse trend is not only observed between Zn/Ni and V/Mn, but also with Ni/Mn, V/Co, and Ni/Cr ratios (Fig. 6). It is noted that the Zn/Ni, Zn/V, and Co/Ni ratios increase progressively, whereas V/Mn, Ni/Mn, V/Co, and Ni/Cr ratios decrease gradually from Mag-1 through Mag-2 to Mag-3 (Fig. 6).

Whole-rock compositions of the monzodiorite

Whole rock compositions of the monzodiorite samples (n=5) are listed in appendix table A2. The least altered samples of monzodiorite have 59.6–60.0 wt.% SiO_2, 16.5–16.9 wt.% Al_2O_3, 2.4–2.8 wt.% MgO, 5.1–6.2 wt.% Na_2O, 3.4–4.1 wt.% K_2O, 3.4–4.2 wt.% CaO, and 4.5–5.1 wt.% FeO_{total}. These samples contain 10.8-14.5 ppm Co (avg.= 12.4) with Co/Fe ratio ranging from 290×10^{-6} to 364×10^{-6} (avg. $=333\times10^{-6}$). The average Co/Fe ratio of the monzodiorite samples are comparable to that of the Fe skarn associated with magmatic rocks from the Handan-Xingtai district (avg. Co/Fe $=351\times10^{-6}$, n=35; Sun et al., 2019b) but are lower than that of the bulk continental crust (avg. Co/Fe ratio $=511\times10^{-6}$; Rudnick and Gao et al., 2003).

DISCUSION

Efficient Fe precipitation

Iron solubility in hydrothermal fluids is sensitive to temperature, salinity and acidity (Chou and Eugster, 1977; Whitney et al., 1985; Kwak et al., 1986; Simon et al., 2004). For chloride solutions equilibrated with granitoid rocks, Whitney et al. (1985) experimentally demonstrated that a temperature decrease from 500 to 400 °C can cause a tenfold decrease in the Fe concentration, whereas a threefold decrease in fluid salinity produces a commensurate decrease in the Fe concentration as temperature decreases from 600 to 400 °C. Additionally, the experimental and theoretical studies of Chou and Eugster (1977) showed that a tenfold decrease in the acid concentration

(mHCl) would produce a hundredfold decrease in the Fe concentration ($mFeCl_2$) in supercritical chloride solutions equilibrated with magnetite. Therefore, ore fluids in Fe skarn systems ought to precipitate a major part of their Fe in response to: (1) cooling as fluids move across steep geothermal gradients in the contact zone (e.g., Meinert et al., 2005); (2) mixing with meteoric water with consequent decreases in temperature and salinity (e.g., Pons et al., 2009); and (3) neutralization of acidic fluids by reaction with enclosing marble (Holser and Schneer, 1961). Collectively, these factors facilitate efficient Fe precipitation. The Fe-phases precipitated from ore fluids can be oxides, silicates, sulfides, or carbonates depending on the activities of oxygen, silica, sulfur, and carbon dioxide in the fluids (Whitney et al., 1985). In the case of the Baijian Fe-(Co) skarn deposit, the gangue consists of Mg-rich silicates such as diopsidic pyroxene, tremolite, and serpentine that contain minor Fe. More importantly, these minerals are volumetrically minor relative to magnetite in the ore bodies (Fig. 2). Other Fe-bearing phases such as hematite, siderite, and pyrite are all subordinate and only locally present. Thus, most of the Fe in the ore fluids precipitated as magnetite during formation of the Baijian Fe-(Co) deposit.

Modeling of trace element fractionation in magnetite

Among the physiochemical parameters, fluid composition is considered to be the primary factor controlling trace element chemistry of magnetite (Nadoll et al., 2014). As magma-derived fluids move through the contact zone, intense magnetite precipitation is expected to occur along the fluid path ways (Fig. 7). High degree

fractional crystallization of magnetite would have progressively modified the fluid composition and therefore the chemical composition of magnetite crystallized. To evaluate the effect of magnetite precipitation on fluid and mineral chemistry in the Baijian Fe-(Co) skarn deposit, we conducted modeling of Rayleigh and equilibrium fractionation. These models assume that hydrothermal fluids exsolved from cooling intrusions are confined by hot marble during skarn formation, which has exceedingly low hydraulic conductivity (Woessner and Poeter, 2020). In the case of Rayleigh fractionation, magnetite crystals are removed from contact with the fluid after they form. In the case of equilibrium fractionation, the fluid remains at all times in equilibrium with magnetite and elements exchange continuously between magnetite and fluid.

Rayleigh and equilibrium fractionation models. Rayleigh fractionation models are formulated using the equations below (the original equation is from Rayleigh, 1896):

$$\frac{C_{fluid}^{j}}{C_{fluid}^{Fe}} \Big/ \frac{C_{fluid}^{j(0)}}{C_{fluid}^{Fe(0)}} = F^{K_d(j)-1}, \quad (1)$$

$$\frac{C_{fluid}^{j}}{C_{fluid}^{i}} \Big/ \frac{C_{fluid}^{j(0)}}{C_{fluid}^{i(0)}} = F^{K_d(j)-K_d(i)}, \quad (2)$$

$$\frac{C_{Mag}^{j}}{C_{Mag}^{Fe}} \Big/ \frac{C_{Mag}^{j(0)}}{C_{Mag}^{Fe(0)}} = F^{K_d(j)-1}, \quad (3)$$

$$\frac{C_{Mag}^{j}}{C_{Mag}^{i}} \Big/ \frac{C_{Mag}^{j(0)}}{C_{Mag}^{i(0)}} = F^{K_d(j)-K_d(i)}, \quad (4)$$

where F is the fraction of Fe in the fluid (1>F>0); *j* and *i* are two trace elements of interests; C_{fluid}^{j}, C_{fluid}^{i}, and C_{fluid}^{Fe} are concentrations of *j*, *i* and Fe in the fluid, respectively; $C_{fluid}^{j(0)}$, $C_{fluid}^{i(0)}$, and $C_{fluid}^{Fe(0)}$ are concentrations of *j*, *i,* and Fe in the initial fluid, respectively; C_{Mag}^{j}, C_{Mag}^{i}, and C_{Mag}^{Fe} are the concentrations *j*, *i*, and Fe

317 in magnetite, respectively; $C_{Mag}^{j(0)}$, $C_{Mag}^{i(0)}$, and $C_{Mag}^{Fe(0)}$ are the concentrations of j, i,
318 and Fe in magnetite equilibrated with the initial fluid, respectively; $K_d(j)$ and $K_d(i)$
319 are the magnetite-fluid distribution coefficients for j and i, which are defined as: $K_d(j)$
320 $= (\frac{C_{Mag}^{j}}{C_{Mag}^{Fe}})/(\frac{C_{fluid}^{j}}{C_{fluid}^{Fe}})$ and $K_d(i) = (\frac{C_{Mag}^{i}}{C_{Mag}^{Fe}})/(\frac{C_{fluid}^{i}}{C_{fluid}^{Fe}})$, respectively.

321 Because of the low abundance of trace elements in hydrothermal magnetite and
322 the stoichiometric control of Fe for this mineral (Nadoll et al., 2014; Dare et al., 2014;
323 Wen et al., 2017), C_{Mag}^{Fe} and $C_{Mag}^{Fe(0)}$ are assumed to be equal. Equation (3) can then
324 be reduced to:

325 $$C_{Mag}^{j}/C_{Mag}^{j(0)} = F^{K_d(j)-1}. \quad (5)$$

326 In the Rayleigh fractionation model, equations (1) and (2) respectively describe the
327 variation of j/Fe and j/i ratios in the fluid, whereas equations (4) and (5) respectively
328 describe the variation of the j/i ratio and j content in magnetite.

329 The equilibrium fractionation models are formulated using the equations (e.g.,
330 Sharp, 2007):

331 $$\frac{C_{fluid}^{j}}{C_{fluid}^{Fe}} / \frac{C_{fluid}^{j(0)}}{C_{fluid}^{Fe(0)}} = 1/[K_d(j) + F * (1 - K_d(j))], \quad (6)$$

332 $$\frac{C_{fluid}^{j}}{C_{fluid}^{i}} / \frac{C_{fluid}^{j(0)}}{C_{fluid}^{i(0)}} = [K_d(i) + F * (1 - K_d(i))]/[K_d(j) + F * (1 - K_d(j))], \quad (7)$$

333 $$\frac{C_{Mag}^{j}}{C_{Mag}^{Fe}} / \frac{C_{Mag}^{j(0)}}{C_{Mag}^{Fe(0)}} = 1/[K_d(j) + F * (1 - K_d(j))], \quad (8)$$

334 $$\frac{C_{Mag}^{j}}{C_{Mag}^{i}} / \frac{C_{Mag}^{j(0)}}{C_{Mag}^{i(0)}} = [K_d(i) + F * (1 - K_d(i))]/[K_d(j) + F * (1 - K_d(j))]. \quad (9)$$

335 The variable definitions in equations (6-9) are the same as those in the previous
336 equations described above. Given that C_{Mag}^{Fe} equals $C_{Mag}^{Fe(0)}$, equation (8) can be
337 simplified to:

338 $$C_{Mag}^{j}/C_{Mag}^{j0} = 1/[K_d(j) + (1 - K_d(j)) * F]. \quad (10)$$

339 In the equilibrium fractionation model, equations (6) and (7), respectively, describe
340 the variation of *j*/Fe and *j/i* ratios in the fluid, whereas equations (9) and (10),
341 respectively, describe the variation of the *j/i* ratio and *j* content in magnetite.

342 **Fractionation of V, Cr, Mn, Co, Ni, and Zn in magnetite.** The following
343 elements, V, Cr, Mn, Co, Ni and Zn, were selected for modeling because: (1) They are
344 among the main discrimination elements for magnetite from various settings (Nadoll
345 et.al., 2014) and their concentrations in magnetite are generally above the detection
346 limits of LA-ICP-MS; (2) Their concentrations are low in the host dolomitic
347 limestone and limestone as well as in the gangue minerals such as diopsidic pyroxene,
348 tremolite, phlogopite, and serpentine (Wen, 2017), such that fluid-rock reactions and
349 the precipitation of gangue minerals has a limited influence on the budget of these
350 elements in the hydrothermal fluid; and (3) The distribution coefficients for these
351 elements between magnetite and chloride solutions are available (Ilton and Eugster,
352 1989; Tauson et al., 2015, 2017; Smagunov et al., 2021).

353 The experimental investigation of Ilton and Eugster (1989) showed that Mn and
354 Zn are incompatible relative to Fe in magnetite in equilibrium with chloride solutions
355 at 600 to 800 °C and 200 MPa. Recent experimental partitioning studies by Tauson et
356 al. (2015, 2017) and Smagunov et al. (2021) confirmed the incompatibility of Mn and
357 Zn along with Co in magnetite equilibrated with chloride solutions at 450 °C and 100
358 MPa with the oxygen fugacity (fO_2) close to the magnetite-hematite buffer.
359 Corresponding distribution coefficients are as follows: K_d(Mn) = 0.009 ± 0.002;
360 K_d(Zn) =0.0017 ± 0.0008; and K_d(Co) = 0.16 ± 0.07. Their experiments further

361 demonstrate the high compatibilities of V and Ni and similar compatibility of Cr
362 relative to Fe in magnetite with distribution coefficients of K_d(V) = 6.6 ± 3.8; K_d(Ni)
363 = 3 ± 1.5; and K_d(Cr) = 1.2 ± 1. We used the mean distribution coefficients for V, Cr,
364 Mn, Co, Ni, and Zn between magnetite and fluid from Tauson et al. (2015, 2017) and
365 Smagunov et al. (2021) for the Rayleigh and equilibrium fractionation modeling. The
366 P, T, and fO_2 conditions for these distribution coefficients are comparable to those
367 during magnetite mineralization at Baijian (Wen 2017) and other skarn Fe deposits
368 worldwide (e.g., Meinert, 1984; Rose et al., 1985; Pons et al., 2009; Li et al., 2019).
369 In both the Rayleigh and equilibrium fractionation models, Mn, Zn, and Co
370 concentrations increase slowly as magnetite precipitation proceeds (Fig. 8A, C). The
371 modeling results are consistent with the trace element compositions of magnetite from
372 the Baijian Fe-(Co) skarn deposit that show a slight increase in the average Mn and
373 Zn concentrations from early Mag-1 to late Mag-3 (Fig. 5). The average concentration
374 of Co increases from Mag-1 to Mag-2 but decreases from Mag-2 to Mag-3 coexisting
375 with pyrite (Figs. 3E-F; Fig. 5), which suggests that pyrite fixes Co more efficiently
376 than magnetite (Dare et al., 2012, 2014; Zhao and Zhou, 2015). It is noteworthy that
377 decreasing temperature generally results in decreasing trace element abundances in
378 magnetite (Dare et al., 2014). Independent evidence that temperature decreased during
379 precipitation of Mag-1 to Mag-3 is provided by decreases in the Ti concentration of
380 magnetite (Fig. 5), which can be used as a proxy for temperature (Dare et al., 2014).
381 The measured increases in the concentration of incompatible Mn, Zn, and Co from
382 Mag-1 to Mag-2/Mag-3 suggests that the effects of magnetite fractional crystallization

were greater than cooling. In contrast, the Cr concentration of magnetite is insensitive to magnetite fractional crystallization in both of the models (Fig. 8A, C). Thus, the measured decrease in the Cr concentration from Mag-1 to Mag-3 is probably due to decreasing temperature.

The compatible elements, V and Ni, in magnetite behave differently between the two models, with their concentrations decreasing more rapidly by Rayleigh fractionation than by equilibrium fractionation (Fig. 8A, C). In the Baijian deposit, the sharp decrease in the concentration of V and Ni from Mag-1 to Mag-3 (more than 2 orders of magnitude different; Fig. 5) is best explained by Rayleigh fractionation (Fig. 8A), because with 60% of the Fe in the fluid consumed by magnetite precipitation there is over a hundred-fold decrease in the concentration of V in the magnetite (calculated with K_d(V) = 6.6; Fig. 8A). It is worth noting that if the maximum distribution coefficient for V (K_d(V) =10.4) is applied in Rayleigh fractionation modeling, achieving such a hundred-fold decrease in V concentration in the magnetite would only require 40% of the Fe to be consumed by magnetite precipitation. Alternatively, the decrease in V and Ni from Mag-1 to Mag-3 may be attributed to a decrease in temperature, though the extent to which temperature affects abundances of V and Ni in the magnetite would require further experimental studies.

Compared to their abundances, the ratios of trace elements in magnetite are much less affected by temperature (Ilton and Eugster, 1989; Smagunov et al., 2021) and thus, most likely, reflect variations in the fluid chemistry. In our samples, the ratios of incompatible to compatible elements, such as Co/Ni, Zn/Ni, and Zn/V, and

compatible to incompatible elements, such as V/Mn, Ni/Mn, and Ni/Cr, remain relatively constant in Mag-1 when compared to Ti (Fig. 9). However, these ratios vary over 2 to 4 orders of magnitude in Mag-2 and Mag-3 as Ti has a narrow range of concentrations (Fig. 9). Since a narrow range in Ti concentrations is indicative of a narrow temperature range, the large variations in metal cation ratios for Mag-2 and Mag-3 must be due to changing metal cation ratios in the fluid. As Mag-2 and Mag-3 represent the main stages of magnetite mineralization, the ore fluids must have undergone high degrees of magnetite precipitation during these stages. During Rayleigh fractionation (Fig. 8B), once 90% of the Fe had precipitated as magnetite there is a circa thousand-fold increase in the Zn/Ni and Co/Ni ratios in the residual fluid and magnetite. Raleigh fractionation can, therefore, explain the large range of metal ratios in Mag-2 and Mag-3. In comparison, equilibrium fractionation is less efficient in fractionating the metal ratios in magnetite (Fig. 8D). Overall, there are obvious trends of increasing incompatible/compatible element ratios (e.g., Co/Ni, Zn/V and Zn/Ni; Fig.6) and decreasing compatible/incompatible element ratios (e.g., V/Mn, Ni/Mn and V/Co, Fig. 6) from Mag-1 to Mag-3. These ratios are strongly correlated with each other (Fig. 6). Such trends and correlations are best explained by increasing degrees of magnetite fractional crystallization.

IMPLICATIONS

Interpretations of magnetite trace element data

Previous studies have suggested that the trace element composition of

hydrothermal magnetite is mainly controlled by fluid chemistry, temperature, oxygen fugacity, fluid-rock interactions, and co-precipitation of other minerals (Dare et al., 2012, 2014; Nadoll et al., 2014). Based on such relationships, magnetite trace element geochemistry has been used to decipher the properties and evolution of magnetite-forming fluids. In this study, we further demonstrate that efficient magnetite precipitation is a significant process leading to large variations in its trace element composition. Such a process should not be overlooked in interpreting magnetite trace element data, especially in hydrothermal systems that generate magnetite-rich ores such as Fe skarn, IOCG, and IOA deposits. For example, a decreasing V concentration in magnetite has been interpreted to reflect the increasing fO_2 of the ore-forming fluids. Alternatively, a decreasing magnetite V concentration can be readily explained by progressive precipitation of magnetite. Similarly, low Ni/Cr ratios (< 1, Dare et al., 2014) and high Co/Ni values (Acosta-Góngora, et al. 2014) are considered indicators for magnetite of igneous origin and magnetite associated with Cu-U (±Co) Fe oxide breccia systems, respectively. However, they are also typical for magnetite that crystalized from a fluid that underwent intense magnetite precipitation, as exemplified by the Baijian Fe skarn (e.g., majority of Mag-3, Figs. 6B and F, Table A1), and therefore could be interpreted differently.

Cobalt mineralization in Fe skarns

Pyrite, which is the main host of Co in the Baijian Fe-(Co) deposit, is paragenetically later than the main stage of magnetite mineralization (Wen, 2017).

449 Because magnetite preferentially consumes Fe over Co from ore fluids as magnetite
450 precipitates, the Co/Fe ratio of the residual fluid increases. In the Rayleigh
451 fractionation model, precipitation of 90% of the Fe in magnetite produces about a
452 seven-fold increase in the Co/Fe ratio of the fluid (Equation 1; Fig. 7A). High fluid
453 Co/Fe ratios would facilitate substitution of Co for Fe in pyrite via the reaction: Co^{2+}
454 + FeS_2 (pyrite) → Fe^{2+} + (Fe, Co)S_2 (Co-rich pyrite). Cobalt sulfides may form when
455 the fluid is exhausted in Fe or during late-stage hydrothermal recrystallization of
456 Co-rich pyrite (Qiu et al., 2021). Such increases in fluid Co/Fe ratios can explain the
457 common occurrence of Co-rich pyrite and Co sulfides in numerous other Fe skarn
458 deposits around the world (Einaudi et al., 1981; Rose et al., 1985; Meinert et al., 2005;
459 Nimis et al., 2014; Slack et al., 2017; Zhao et al., 2019; Wei et al., 2021; Yan et al.,
460 2021; Shi et al., 2023). Notably, other magnetite-dominant deposit types such as
461 IOCG and IOA deposits also contain appreciable Co-rich sulfides (Williams et al.,
462 2005), such as the Ernest Henry IOCG deposit in the Cloncurry district of Australia
463 (Mark et al., 2000) and the Los Colorados IOA deposit in northern Chile (Reich et al.,
464 2016). These large tonnage deposits contain large amounts of hydrothermal magnetite
465 and small amounts of late stage Co-rich sulfides. This would support our conjecture
466 that magnetite precipitation could play an important role in elevating fluid Co/Fe
467 ratios and the subsequent precipitation of Co-rich sulfides in these
468 magnetite-dominant ore deposits. The formation of Co-rich pyrite and Co sulfides is
469 required for economic Co exploitation.

470 The average Co/Fe ratio of magnetite (Co/Fe = $83*10^{-6}$; Table A1) and the

magnetite-fluid Co/Fe partition coefficient ratio (K_d(Co) = 0.16±0.07; Smagunov et al. 2021), were used to calculate the average Co/Fe ratio for the Baijian ore fluid of (517±226) $*10^{-6}$, which is comparable to that of the monzodiorite (avg. $333*10^{-6}$, represented by the average values of the least altered samples, Table A2). This consistency indicates that Co/Fe fractionation between aqueous fluids and magmas is insignificant, as suggested by Williams-Jones and Vasyukova (2022). If the magmatic fluids that form Fe skarns have Co/Fe ratios that are similar to those of related plutons, then deposits with significant Fe reserves (>50 Mt Fe) have the potential to contain substantial amounts of Co. In the case of Baijian, mass balance calculations suggest that the 53.3 Mt of Fe (112 Mt ore at 47.6 wt.% Fe) in this deposit may contain 17,749 t of Co. This calculated Co content is close to the Baijian deposit's Co reserve (17,186 t), approximately 1/40 of global Co reserves (700,000 t; USGS, 2020). Our findings underscore the importance of assessing Co resources in Fe skarn deposits, as they can potentially contribute significant production to meet the ongoing demand for this metal.

FUNDINGS AND ACKNOWLEDGMENTS

This study was financially supported by the National Key Research and Development Program of China (No. 2023YFF0804200) and the National Natural Science Foundation of China (No. 42172101; No. 42321001; No. 41802114). We thank Xiaodong Deng, Xiaoye Jin, Yang Li, Yi Sun, Yaoqian Wu and Ming Bai for their help during the fieldwork. We thank U.S. Geological Survey reviewer Corey

Meighan for comments and suggestions. Insightful reviews provided by Dr. Michael Anenburg and an anonymous reviewer are greatly appreciated, which significantly enhanced this manuscript. Editorial handling by Dr. Denis Fougerousse is acknowledged. Any use of trade, product, or firm names is for descriptive purposes only and does not imply endorsement by the U.S. Government.

REFERENCES CITED

Acosta-Góngora, P., Gleeson, S.A., Samson, I.M., Ootes, L., and Corriveau, L. (2014) Trace element geochemistry of magnetite and its relationship to Cu-Bi-Co-Au-Ag-UW mineralization in the Great Bear magmatic zone, NWT, Canada. Economic Geology, 109, 1901–1928.

Canil, D., and Lacourse, T. (2020) Geothermometry using minor and trace elements in igneous and hydrothermal magnetite. Chemical Geology, 541, 119576.

Canil, D., Grondahl, C., Lacourse, T., and Pisiak, L.K. (2016) Trace elements in magnetite from porphyry Cu‐Mo‐Au deposits in British Columbia, Canada. Ore Geology Reviews, 72, 1116-1128.

Chen, B., Jahn, B.M., Arakawa, Y., and Zhai, M.G. (2004) Petrogenesis of the Mesozoic intrusive complexes from the southern Taihang Orogen, North China Craton: Elemental and Sr‐Nd‐Pb isotopic constraints. Contribution to Mineralogy and Petrology. 148, 489-501.

Chen, B., Tian, W., Jahn, B.M., and Chen, Z.C. (2008) Zircon SHRIMP U‐Pb ages and in-situ Hf isotopic analysis for the Mesozoic intrusions in South Taihang,

North China craton: Evidence for hybridization between mantle-derived magmas and crustal components. Lithos, 102, 118-137.

Chou, I., and Eugster, H.P. (1977) Solubility of magnetite in supercritical chloride solutions. American Journal of Science, 277, 1296-1314.

Dare, S.A., Barnes, S., and Beaudoin, G. (2012) Variation in trace element content of magnetite crystallized from a fractionating sulfide liquid, Sudbury, Canada: Implications for provenance discrimination. Geochimica et Cosmochimica Acta, 88, 27-50.

Dare, S.A., Barnes, S., Beaudoin, G., Méric, J., Boutroy, E., and Potvin-Doucet, C. (2014) Trace elements in magnetite as petrogenetic indicators. Mineralium Deposita, 49, 785- 796.

Dare, S.A., Barnes, S. and Beaudoin. G. (2015) Did the massive magnetite"lava flows" of El Laco (Chile) form by magmatic or hydrothermal processes? New constraints from magnetite composition by LA-ICP-MS. Mineralium Deposita, 50, 607-617.

Deng, X., Li, J. and Wen, G. (2015) U-Pb geochronology of hydrothermal zircons from the early cretaceous iron skarn deposits in the Handan-Xingtai district, north china craton. Economic Geology, 110, 2159-2180.

Duparc, Q., Dare, S.A., Cousineau, P.A., and Goutier, J. (2016) Magnetite chemistry as a provenance indicator in archean metamorphosed sedimentary rocks. Journal of Sedimentary Research, 86, 542-563.

Dupuis, C. and Beaudoin, G. (2011) Discriminant diagrams for iron oxide trace

element fingerprinting of mineral deposit types. Mineralium Deposita, 46, 319-335.

Einaudi, M.T., Meinert, L.D., and Newberry, R.J. (1981) Skarn Deposits: Economic Geology 75th Anniversary Volume 317–391.

Gast, P.W. (1968) Trace element fractionation and the origin of tholeiitic and alkaline magma types. Geochimica et Cosmochimica Acta, 32, 1057-1086.

Grigsby, J.D. (1990) Detrital magnetite as a provenance indicator. Journal of Sedimentary Research, 60, 940-951.

Holser, W.T., and Schneer, C.J. (1961) Hydrothermal magnetite. GSA Bulletin, 72, 369-385.

Hu, H., Li, J., Lentz, D., Ren, Z., Zhao, X., Deng, X., and Hall, D. (2014) Dissolution−reprecipitation process of magnetite from the Chengchao iron deposit: Insights into ore genesis and implication for in-situ chemical analysis of magnetite. Ore Geology Reviews, 57, 393-405.

Huang, X.W. and Beaudoin, G. (2019) Textures and chemical compositions of magnetite from iron oxide Copper-Gold (IOCG) and Kiruna-Type iron Oxide-Apatite (IOA) deposits and their implications for ore genesis and magnetite classification schemes. Economic Geology, 114, 953-979.

Huang, X.W., Boutroy, É., Makvandi, S. Beaudoin, G., Corriveau, L., and De Toni, A.F. (2018) Trace element composition of iron oxides from IOCG and IOA deposits: Relationship to hydrothermal alteration and deposit subtypes. Mineralium Deposita, 54, 525-552

560 IGSNC and HGI (Institute of Geological Sciences of North China and Hebei
561 Geological Institute) (1976) Exploration Report on Handan-Xingtai type Iron
562 Deposits in the Taihang Mountain Areas, People's Republic of China:
563 Shijiazhuang, 154 P. (in Chinese).
564 Ilton, E.S., and Eugster, H.P. (1989) Base metal exchange between magnetite and a
565 chloride-rich hydrothermal fluid. Geochimica et Cosmochimica Acta, 53,
566 291-301.
567 Knipping, J.L., Bilenker, L.D., Simon, A.C., Reich, M., Barra, F., Deditius, A.P.,
568 Lundstrom, C., Bindeman, I., and Munizaga, R. (2015) Giant Kiruna-type
569 deposits form by efficient flotation of magmatic magnetite suspensions. Geology,
570 43, 591-594.
571 Kwak, T., Brown, W.M., Abeysinghe, P.B., and Tan, T.H. (1986) Fe solubilities in
572 very saline hydrothermal fluids; Their relation to zoning in some ore deposits.
573 Economic Geology, 81, 447-465.
574 Li. W., Xie, G., Mao, J. Zhu, Q., and Zheng, J. (2019) Mineralogy, fluid inclusion,
575 and stable isotope studies of the chengchao deposit, Hubei province, eastern
576 china: Implications for the formation of high-grade Fe skarn deposits. Economic
577 Geology, 114, 325-352.
578 Lindsley, D.H. (1991) Experimental studies of oxide minerals. Reviews in
579 Mineralogy and Geochemistry, 25, 69-106.
580 Longerich HP, Jackson SE, and Gunther D (1997) Laser ablation inductively coupled
581 plasma mass spectrometric transient signal data acquisition and analyte

582 concentration calculation. Journal of Analytical Atomic Spectrometry, 11, 899–
583 904.
584 Luo, T., Zhang, H., Wu, J., Zhou, X., and Zhang, L. (2022) Magma Generation of
585 Magnetite-Rich Intermediate-Mafic Rocks and Its Mantle Processes in the
586 Southwestern Alxa Block, NW China. Journal of Earth Science, 33(1), 161-176.
587 Mark, G., Oliver, N.H.S., Williams, P.J., Valenta, R.K., and Crookes, R.A. (2000)
588 The evolution of the Ernest Henry Fe-oxide-(Cu-Au) hydrothermal system, in
589 Porter, T.M., ed., Hydrothermal iron oxide copper-gold & related deposits-A
590 global perspective: Adelaide, South Australia, Australia, PGC Publishing, v. 1, p.
591 123–136.
592 Meinert, L.D. (1984) Mineralogy and petrology of iron skarns in western British
593 Columbia, Canada. Economic Geology, 79, 869-882.
594 Meinert, L.D., Dipple, G.M., and Nicolescu, S. (2005) World skarn deposits. In
595 Economic Geology 100th Anniversary Volume, (eds. J. W. Hedenquist, J. F. H.
596 Thompson, R. J. Goldfarb and J. P. Richards). pp. 299–336.
597 Nadoll, P., and Koenig, A.E. (2011) LA-ICP-MS of magnetite: Methods and
598 reference materials. Journal of Analytical Atomic Spectrometry, 26, 1872-1877.
599 Nadoll, P., Mauk, J.L., Hayes, T.S., Koenig, A.E., and Box, S.E. (2012) Geochemistry
600 of magnetite from hydrothermal ore deposits and host rocks of the
601 Mesoproterozoic Belt Supergroup, United States. Economic Geology, 107,
602 1275-1292.
603 Nadoll, P., Angerer, T., Mauk, J.L., French, D., and Walshe, J. (2014) The chemistry

of hydrothermal magnetite: A review. Ore Geology Reviews, 61, 1-32.

Nimis, P., Dalla Costa, L., and Guastoni, A. (2014) Cobaltite-rich mineralization in the iron skarn deposit of Traversella (Western Alps, Italy). Mineralogical Magazine, 78, 11-27.

Pisiak L.K., Canil, D., Lacourse, T., Plouffe, A., and Ferbey, T. (2017) Magnetite as an indicator mineral in the exploration of porphyry deposits: A case study in till near the mount polley Cu-Au deposit, british columbia, Canada. Economic Geology, 112, 919-940.

Pons, J.M., Franchini, M., Meinert, L., Recio, C., and Etcheverry, R. (2009) Iron skarns of the Vegas Peladas District, Mendoza, Argentina. Economic Geology, 104, 157-184.

Qiu, Z., Fan, H., Goldfarb, R., Tomkins, A.G., Yang, K., Li, X., Xie, L., and Liu, X. (2021) Cobalt concentration in a sulfidic sea and mobilization during orogenesis: Implications for targeting epigenetic sediment-hosted Cu-Co deposits. Geochimica et Cosmochimica Acta, 305, 1-18.

Rayleigh J.W.S. (1986) Theoretical considerations respecting the separation of gases by diffusion and similar processes. The London, Edinburgh and Dublin Philosophical Magazine and Journal of Science, 42, 493-498.

Reich, M., Simon, A.C., Barra, F., Palma, G., Hou, T., and Bilenker, L.D. (2022) Formation of iron oxide – apatite deposits. Nature Reviews Earth & Environment, 3, 758–775.

Reich, M., Simon, A.C., Deditius, A., Barra, F., Chryssoulis, S., Lagas, G., Tardani,

D., Knipping, J., Bilenker, L., Sánchez-Alfaro, P., Roberts, M.P., and Munizaga, R. (2016) Trace element signature of pyrite from the los colorados iron oxide-apatite (IOA) deposit, chile: A missing link between andean IOA and iron oxide copper-gold systems? Economic Geology, 111, 743-761.

Rose, A.W., Herrick, D.C., and Deines P. (1985) An oxygen and sulfur isotope study of skarn-type magnetite deposits of the Cornwall type, southeastern Pennsylvania. Economic Geology, 80 (2), 418–443.

Rudnick, R.L., and Gao, S. (2003) Composition of the continental crust. Treatise on Geochemistry, 3, 1–65.

Sharp, Z. (2007) Principles of Stable Isotope Geochemistry. Prentice Hall, Pearson.

Shen, J., Santosh, M., Li, S., Zhang, H., Yin, N., Dong, G., Wang, Y., Ma, G., and Yu, H. (2013) The Beiminghe skarn iron deposit, eastern China: Geochronology, isotope geochemistry and implications for the destruction of the North China Craton. Lithos 156-159: 218-229.

Shi, L., Zhou, T., Fan, Y., Zhang Y., Yan L., Liang X. (2023) Evaluation on the current status and comprehensive utilization prospect of associated cobalt resources in the Middle-Lower Yangtze River Valley metallogenic belt. Acta Petrologica Sinica, 39(4), 1144-1156 (in Chinese).

Simon, A.C., Pettke, T., Candela, P.A., Piccoli, P.M., and Heinrich, C.A. (2004) Magnetite solubility and iron transport in magmatic-hydrothermal environments. Geochimica et Cosmochimica Acta, 68, 4905-4914.

Slack. J.F., Kimball, B.E., and Shedd, K.B. (2017) Cobalt, Chapter F, in Schulz, K.J.,

DeYoung, J.J.H., Seal Ii, R.R., and Bradley, D.C., eds., Critical mineral resources of the United States—Economic and environmental geology and prospects for future supply: U.S. Geological Survey, Professional Paper 1802: p. F1–F40.

Smagunov, N., Tauson, V., Lipko, S., Babkin, D., and Bryansky, N. (2021) Partitioning and surficial segregation of trace elements in iron oxides in hydrothermal fluid systems. Minerals, 11, 57.

Song, Z., Li, H., Li, L., Ding, J., and Meng, J. (2021) Iron isotopes and trace element compositions of magnetite from the submarine Volcanic-Hosted iron deposits in east Tianshan, NW China: New insights into the mineralization processes. Journal of Earth Science, 32, 219-234.

Sun, Y., Wu, T., Xiao, L., Bai, M., and Zhang, Y. (2019a) U-Pb ages, Hf-O isotopes and trace elements of zircons from the ore-bearing and ore-barren adakitic rocks in the Handan-Xingtai district: Implications for petrogenesis and iron mineralization. Ore Geology Reviews, 104, 14-25.

Sun, Y., Wu, T., Xiao, L., Bai, M., and Zhang Y. (2019b) Contrasting mineralogical-geochemical compositions of ore-bearing and ore-barren intrusive complexes in the Handan-Xingtai district, North China Craton: Implications for the iron mineralization. Lithos, 350–351, 105244.

Sun, Y., Xiao, L., Zhu, D., Wu T, Deng, X., Bai, M., and Wen, G. (2014) Geochemical, geochronological, and Sr-Nd−Hf isotopic constraints on the petrogenesis of the Qicun intrusive complex from the Handan−Xingtai district:

Implications for the mechanism of lithospheric thinning of the North China Craton. Ore Geology Reviews, 57, 363-374.

Tauson, V.L., Smagunov, N.V., and Lipko, S.V., (2017) Cocrystallization coefficients of Cr, V, and Fe in hydrothermal ore systems (from experimental data). Russian Geology and Geophysics, 58, 949-955.

Tauson, V.L, Smagunov, N.V., and Lipko, S.V. (2015) Using cocrystallization coefficients of isomorphous admixtures for determination of element concentrations in ore-forming solutions (by the example of Mn/Fe ratio in magnetite). Russian Geology and Geophysics, 56, 1128-1132.

USGS, 2020. Mineral commodity summaries 2020: U.S. Geological Survey, 200 p. https://doi.org/10.3133/mcs2020.

Ward, L.A., Holwellm D.A., and Barry, T.L. (2018) The use of magnetite as a geochemical indicator in the exploration for magmatic Ni-Cu-PGE sulfide deposits: A case study from Munali, Zambia. Journal of Geochemical Exploration, 188, 172-184.

Wei, K., Xu, J., Wu, C., Liu, D., and Yan, F. (2021) Discussion on the current status and comprehensive utilization prospect of cobalt ore resources in ore-concentrated area of southeast Hubei. Resources Environment and Engineering. 35, 777-781 (in Chinese).

Wen, G. (2017) The mechanisms and key factors in forming highgrade iron skarn deposits in Handan-Xngtai district, North China Craton. Ph. D. thesis. China University of Geosciences (Wuhan).

692 Wen, G., Li, J., Hofstra, A.H., Koenig, A.E., and Cui, B. (2020) Textures and
693 compositions of clinopyroxene in an Fe skarn with implications for ore-fluid
694 evolution and mineral-fluid REE partitioning. Geochimica et Cosmochimica
695 Acta, 290, 104-123.
696 Wen, G., Li, J., Hofstra, A.H., Koenig AE, Lowers, H.A., and Adams, D. (2017)
697 Hydrothermal reequilibration of igneous magnetite in altered granitic plutons and
698 its implications for magnetite classification schemes: Insights from the
699 Handan-Xingtai iron district, North China Craton. Geochimica et Cosmochimica
700 Acta, 213, 255-270.
701 Whitney, J.A., Hemley, J.J., and Simon, F.O. (1985) The concentration of iron in
702 chloride solutions equilibrated with synthetic granitic compositions; The
703 sulfur-free system. Economic Geology, 80, 444-460.
704 Williams-Jones, A. E. and Vasyukova, O. V. (2022) Constraints on the Genesis of
705 Cobalt Deposits: Part I. Theoretical Considerations. Economic Geology, 117,
706 513–528.
707 Williams, P.J., Barton, M.D., Johnson, D.A., Fontboté, L., De Haller, A., Mark, G.,
708 Oliver, N.H., and Marschik, R. (2005) Iron oxide copper-gold deposits: Geology,
709 space-time distribution, and possible modes of origin. Economic Geology,
710 371-405.
711 William, W., and Poeter, E., (2020) Hydrogeologic Properties of Earth Materials and
712 Principles of Groundwater Flow. The Groundwater Project, Guelph, Ontario,
713 Canada.

714 Yan, L., Fan Y., and Liu Y. (2021) The occurrence and spatial distribution of cobalt
715 in Longqiao iron deposit in Luzong Basin, Anhui Province. Acta Petrologica
716 Sinica, 37(9), 2778-2790 (in Chinese).
717 Zeng, L., Zhao, X., Spandler, C. Hu, H., Hu, B., Li, J., and Hu, Y. (2022) Origin of
718 high-Ti magnetite in magmatic-hydrothermal systems: Evidence from iron
719 oxide-apatite (IOA) deposits of eastern China. Economic Geology, 117, 923-942.
720 Zhang, S., Chen, H., Xiao, B., Zhao, L., Hu, X., Li, j., and Gong, L.(2023) Textural
721 and chemical evolution of magnetite from the Paleozoic Shuanglong Fe-Cu
722 deposit: Implications for tracing ore-forming fluids. American Mineralogist, 108
723 (1), 178–191.
724 Zhang, Y., Hollings, P., Shao, Y.J., Li, D.F., Chen, H.Y., and Li, H.B. (2020)
725 Magnetite texture and trace-element geochemistry fingerprint of pulsed
726 mineralization in the Xinqiao Cu-Fe-Au deposit, Eastern China. American
727 Mineralogist, 105, 1712–1723.
728 Zhao G., Sun M., Wilde S.A., and Li S. (2005) Late Archean to Paleoproterozoic
729 evolution of the North China Craton: key issues revisited. Precambrian Research,
730 136, 177–202.
731 Zhao, W.W., and Zhou, M. (2015) In-situ LA‐ICP-MS trace elemental analyses of
732 magnetite: The Mesozoic Tengtie skarn Fe deposit in the Nanling Range, South
733 China. Ore Geology Reviews, 65, 872-883.
734 Zhao, Y. M. (2013) Main genetic types and geological characteristics of iron-rich ore
735 deposits in China. Mineral Deposits, 32, 685-704 (in Chinese).

Zhao, J. X., Li G. M, Qin K. Z., and Tang D. M. (2019) A review of the types and ore mechanism of the cobalt deposits. Chinese Science Bulletin, 64, 2484–2500 (in Chinese).

Figure and table captions

Figure 1. Geologic map of the Handan-Xingtai district (IGSNC and HGI, 1976) showing the distribution of Fe skarn deposits and associated granitoid intrusions in Ordovician carbonates. The inset shows the major tectonic units of the North China Craton and the location of the Handan-Xingtai district. Abbreviations: CAOB = Central Asian Orogenic Belt; YZC = Yangtze Craton.

Figure 2. A representative cross section of the Baijian Fe skarn deposit showing drill holes, rock units, and the morphology of the two major orebodies.

Figure 3. Representative photographs showing the textures and mineralogy of the samples used in this study. (A) Sample of massive pyroxene skarn, consisting of over 90 vol.% diopsidic pyroxene. (B-D) Samples of magnetite ores associated with retrograde skarn assemblages. These samples contain variable amount of phlogopite, tremolite and serpentine; (E-F) Samples of magnetite ore associated with sulfides. Pyrite occurs as disseminations within massive magnetite. Calcite veinlets locally replace magnetite. Mineral abbreviations: Px-pyroxene; Mag-magnetite; Phl-phlogopite; Tr-tremolite; Srp-serpentine; Py-pyrite; Cal-calcite.

Figure 4. BSE images showing typical features of magnetite observed in the

759 samples studied. (A) Subhedral magnetite enclosed in a pyroxene crystal; (B-C)
760 Magnetite contains abundant mineral inclusions of apatite and pyroxene; (D-E)
761 Magnetite intergrown with tremolite, which replaces pyroxene; (F) Magnetite and
762 phlogopite replacing pyroxene; (G-I) Magnetite intergrown with serpentine, which
763 locally replaces olivine; (J) Magnetite mantled by pyrite and calcite; (K) Magnetite
764 replaced by calcite and hematite; (L) Calcite and siderite veinlets and replacements in
765 magnetite. Mineral abbreviations: Ap-apatite; Px- pyroxene; Mag-magnetite;
766 Phl-phlogopite; Tr-tremolite; Srp-serpentine; Py-pyrite; Cal-calcite; Ol-Olivine;
767 Hem-hematite; Sid-siderite.

768 Figure 5. Box plot showing the abundance of trace elements in magnetite.

769 Figure 6. Plots of Zn/Ni vs. Zn/V (A), Zn/Ni vs. Co/Ni (B), Zn/Ni vs. V/Mn (C),
770 Zn/Ni vs. /Ni/Mn (D), Zn/Ni vs. V/Co (E), and Zn/Ni vs. Ni/Cr (F). The Zn/Ni ratios
771 are positively correlated with Zn/V and Co/Ni ratios (A-B) and are negatively
772 correlated with V/Mn, Ni/Mn, V/Co, and Ni/Cr ratios (C-F). From Mag-1 through
773 Mag-2 to Mag-3, the Zn/Ni, Zn/V, and Co/Ni ratios increase progressively (A-B),
774 whereas the V/Mn, Ni/Mn, V/Co, and Ni/Cr ratios decrease gradually (C-F).

775 Figure 7. Schematic illustration of ore fluids migrating through the contact zone in
776 the Baijian Fe skarn deposit. The Fe-charged ore fluids undergo significant magnetite
777 precipitation at the initial mineralization front and final mineralization front, which is
778 confined by the marble halo. As magnetite continues to precipitate, the ore fluids
779 undergo progressive Fe depletion with escalating degrees of fractionation between
780 compatible elements (V and Ni) and incompatible elements (Mn, Zn, and Co). These

781 fractionations in the ore fluids are recorded in magnetite formed in the ore zone (T2
782 and T3 magnetite). See the text for further explanation. Abbreviation: Mag-magnetite;
783 Py-pyrite.

784 Figure 8. Rayleigh (A, B) and equilibrium (C, D) curves for trace elements and
785 trace element ratios during magnetite fractional crystallization in a closed system. The
786 magnetite-fluid distribution coefficients for each trace element are assumed to be
787 constant during the fractional crystallization process.

788 Figure 9. Plots of Ti vs. Zn/V (A), Co/Ni (B), V/Mn (C), Ni/Mn (D), V/Co (E),
789 and Ni/Cr (F). These trace element ratios remain relatively constant in Mag-1 but vary
790 over 2 to 4 orders of magnitude in Mag-2 and Mag-3 within a narrow range of Ti
791 concentrations.

792

793 **Appendix**

794 Appendix Table A1. Trace element data of magnetite from the Baijian Fe skarn.
795 Appendix Table A2. Whole-rock major element compositions and Co concentration of
796 the ore-related monzodiorite.

Figure 1

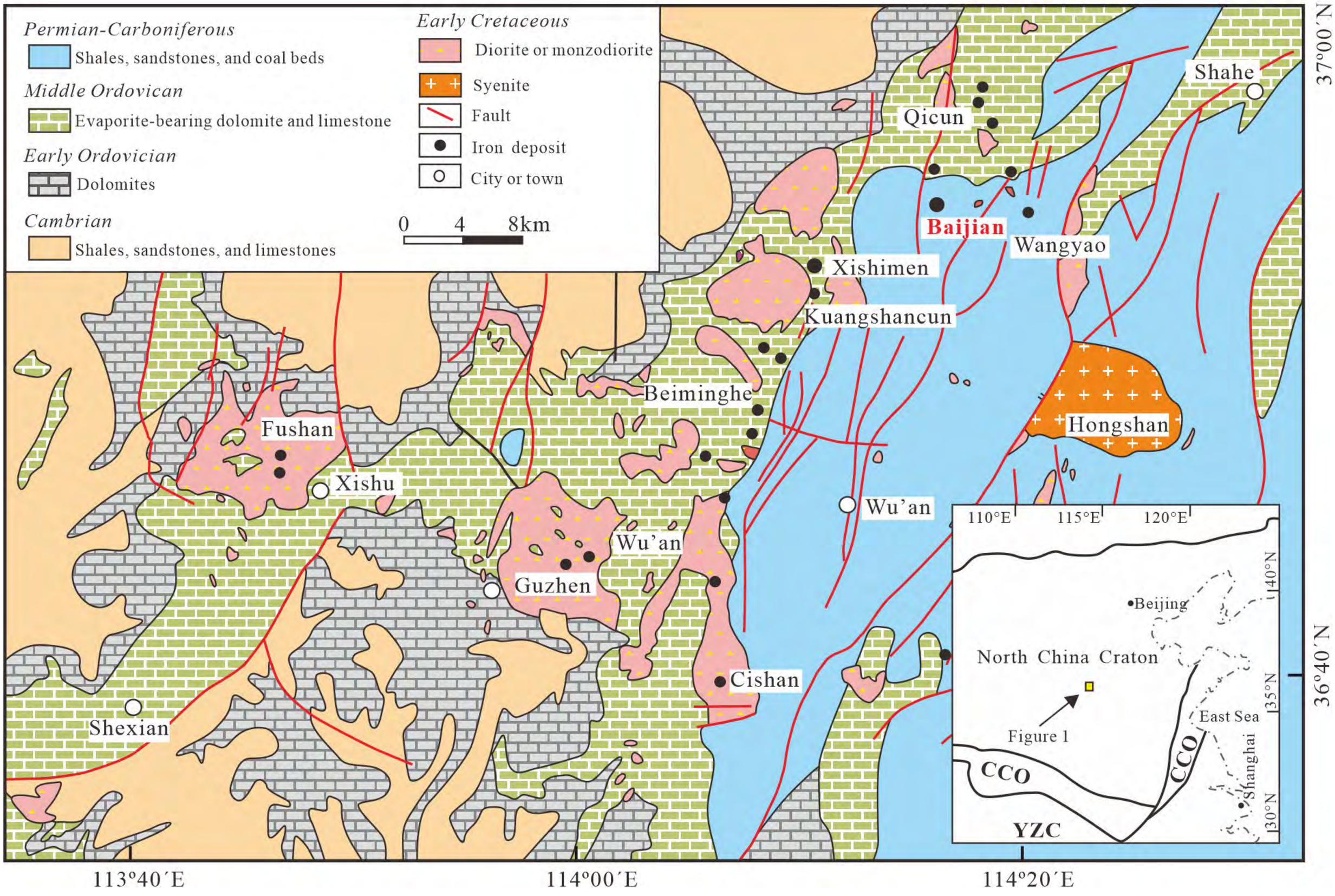
Permian-Carboniferous
Shales, sandstones, and coal beds
Middle Ordovican
Evaporite-bearing dolomite and limestone
Early Ordovician
Dolomites
Cambrian
Shales, sandstones, and limestones
Early Cretaceous
Diorite or monzodiorite
Syenite
Fault
Iron deposit
City or town
0 4 8km
Shahe
Qicun
Baijian
Wangyao
Xishimen
Kuangshancun
Beiminghe
Hongshan
Fushan
Xishu
Wu'an
Guzhen
Wu'an
Cishan
Shexian
37°00′N
36°40′N
113°40′E
114°00′E
114°20′E
110°E
115°E
120°E
40°N
35°N
30°N
Beijing
North China Craton
Figure 1
East Sea
Shanghai
CCO
CCO
YZC

Figure 2

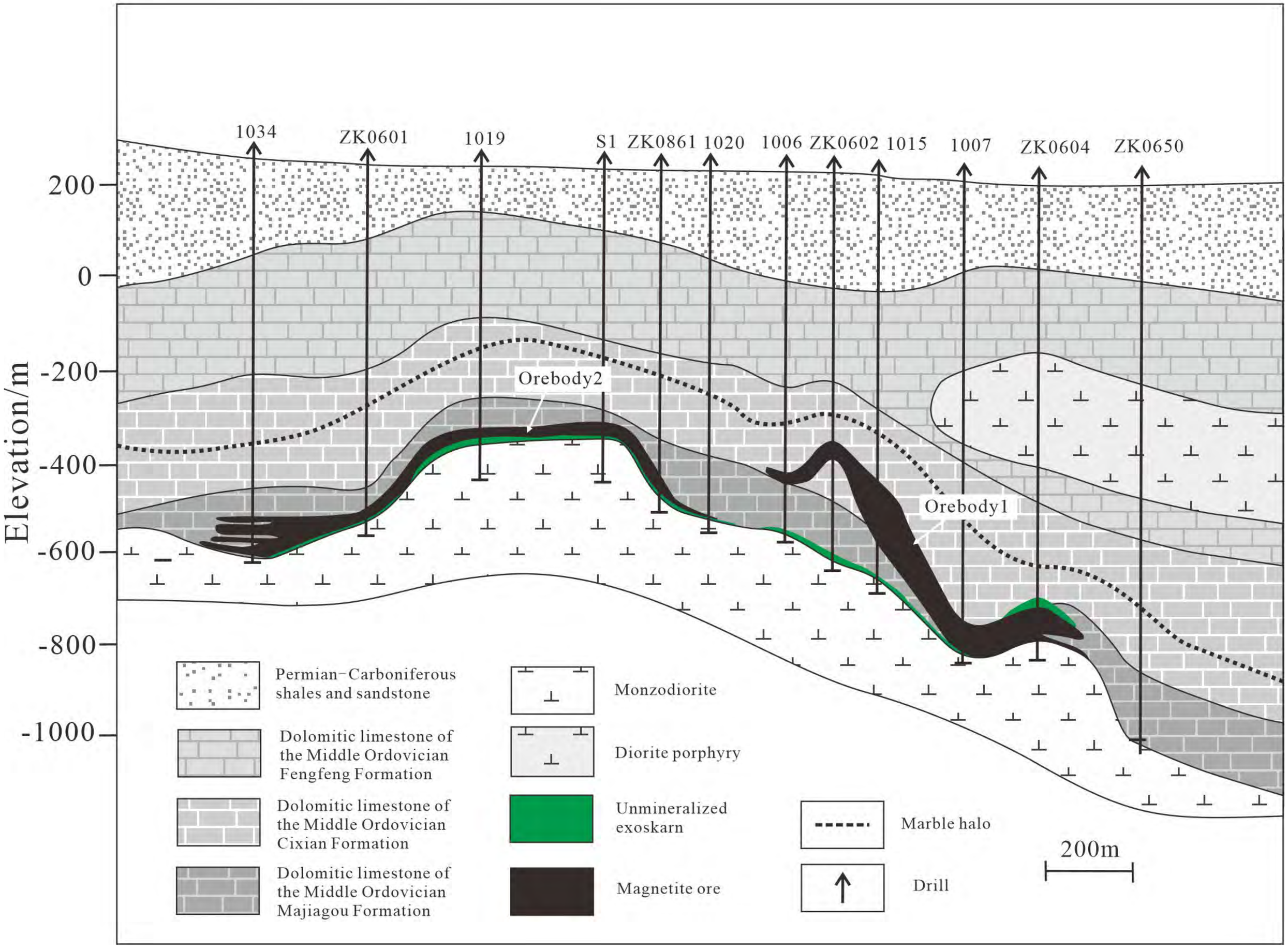
1034
ZK0601
1019
S1
ZK0861
1020
1006
ZK0602
1015
1007
ZK0604
ZK0650
200
0
-200
-400
-600
-800
-1000
Elevation/m
Orebody2
Orebody1
Permian-Carboniferous shales and sandstone
Dolomitic limestone of the Middle Ordovician Fengfeng Formation
Dolomitic limestone of the Middle Ordovician Cixian Formation
Dolomitic limestone of the Middle Ordovician Majiagou Formation
Monzodiorite
Diorite porphyry
Unmineralized exoskarn
Magnetite ore
Marble halo
Drill
200m

Figure 3

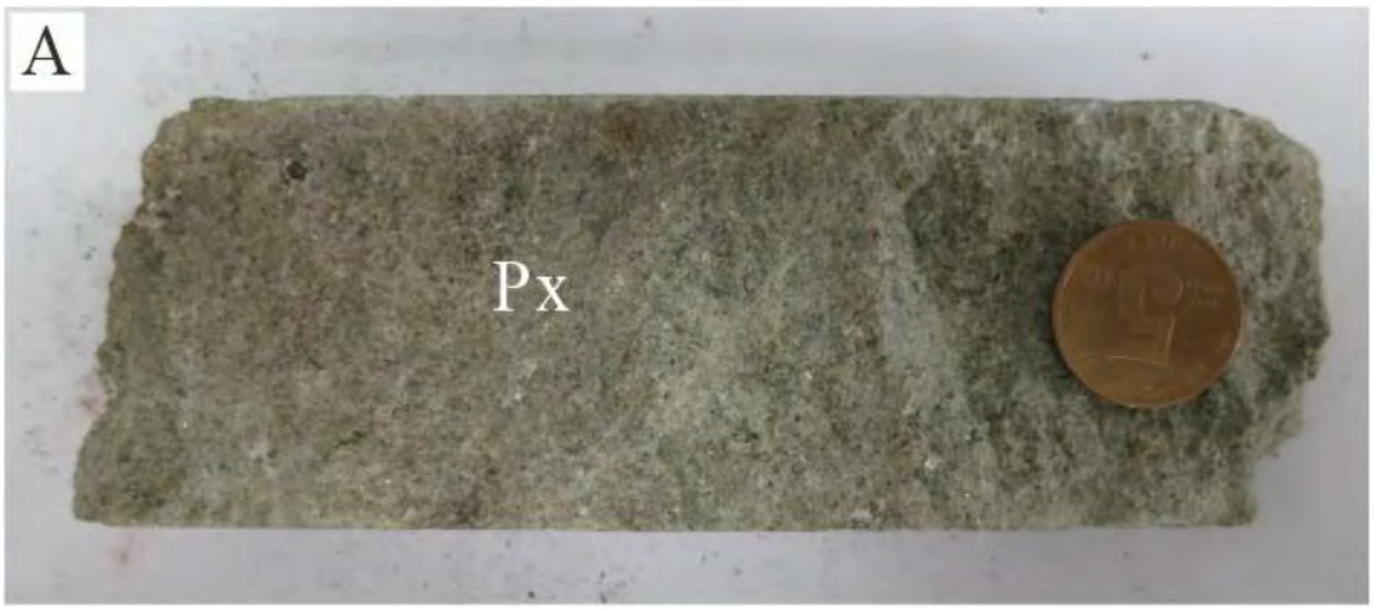

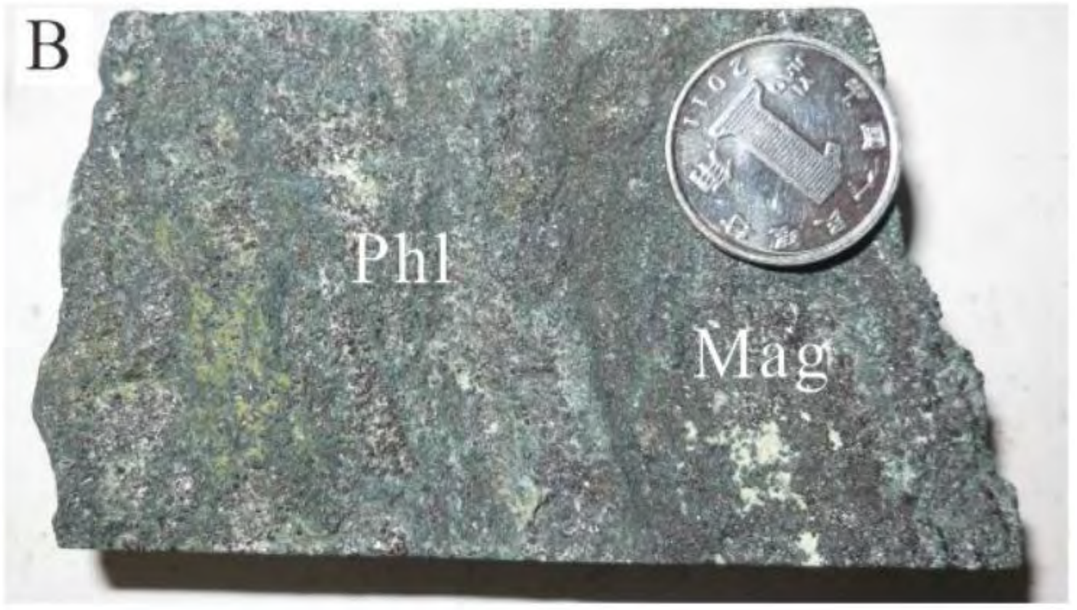

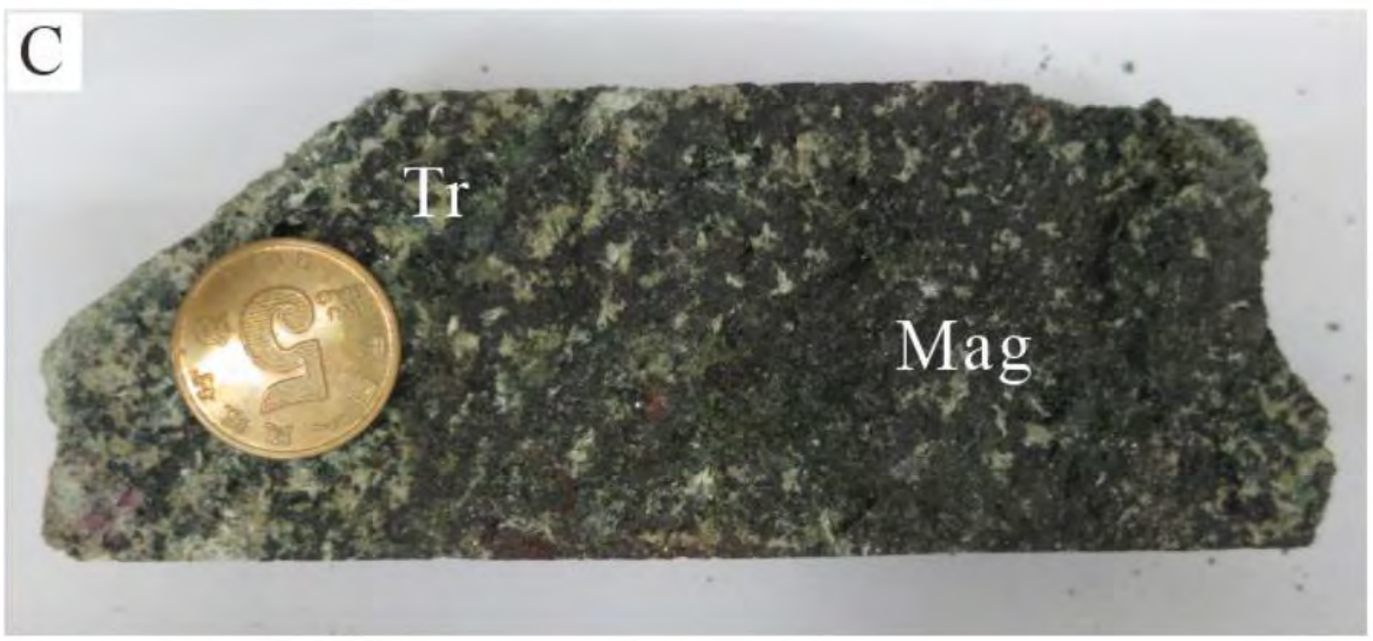

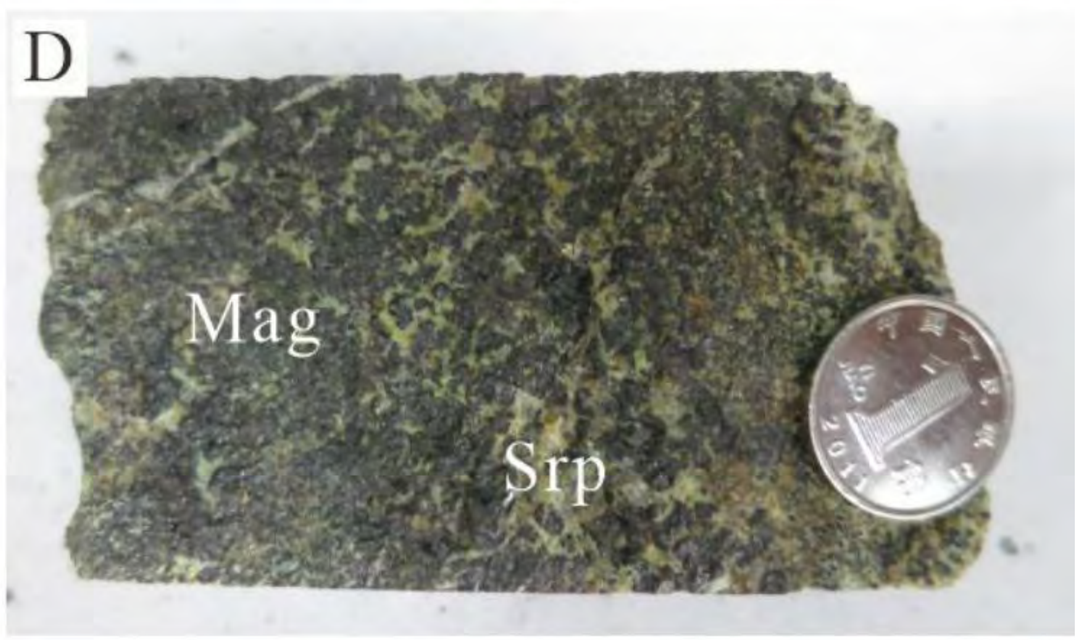

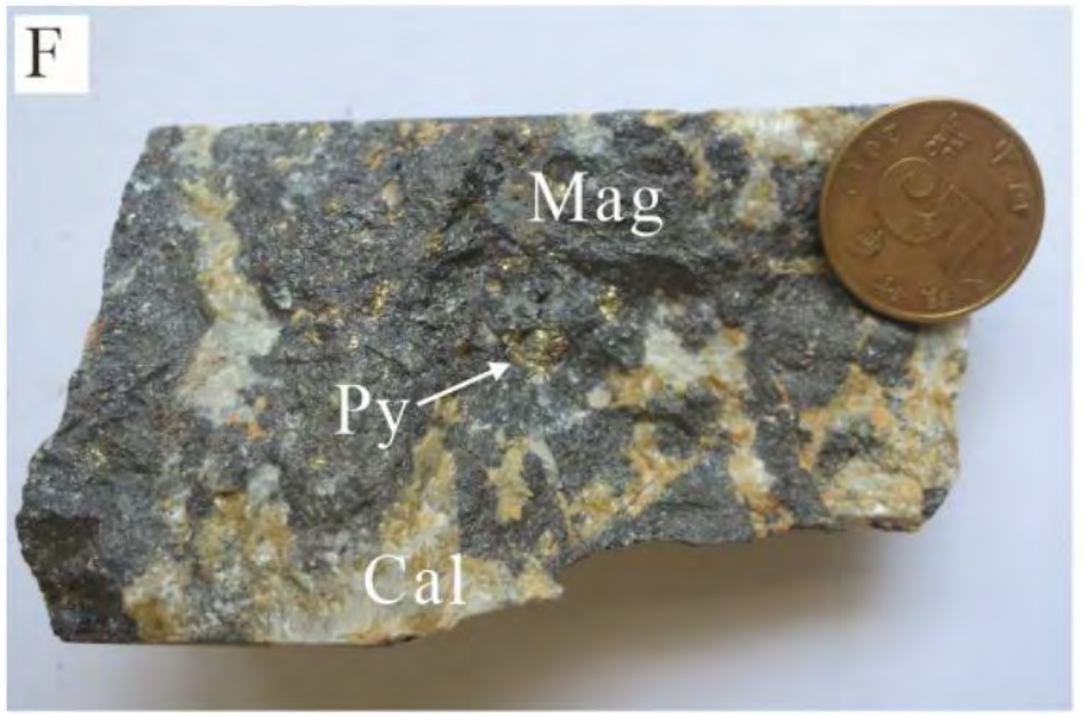

Figure 4

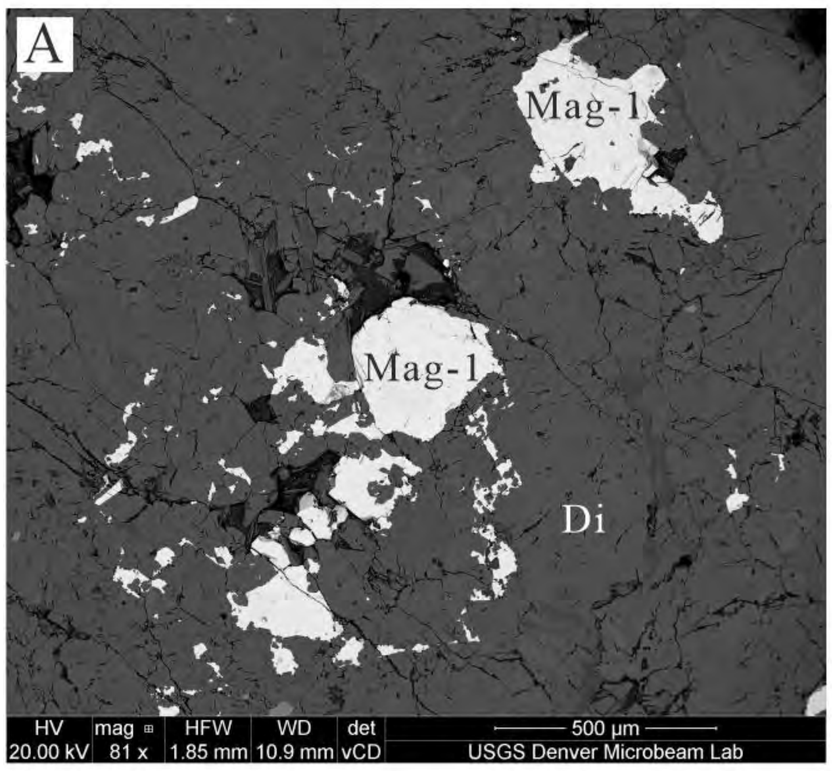
A
Mag-1
Mag-1
Di
HV 20.00 kV
mag 81 x
HFW 1.85 mm
WD 10.9 mm
det vCD
500 µm
USGS Denver Microbeam Lab

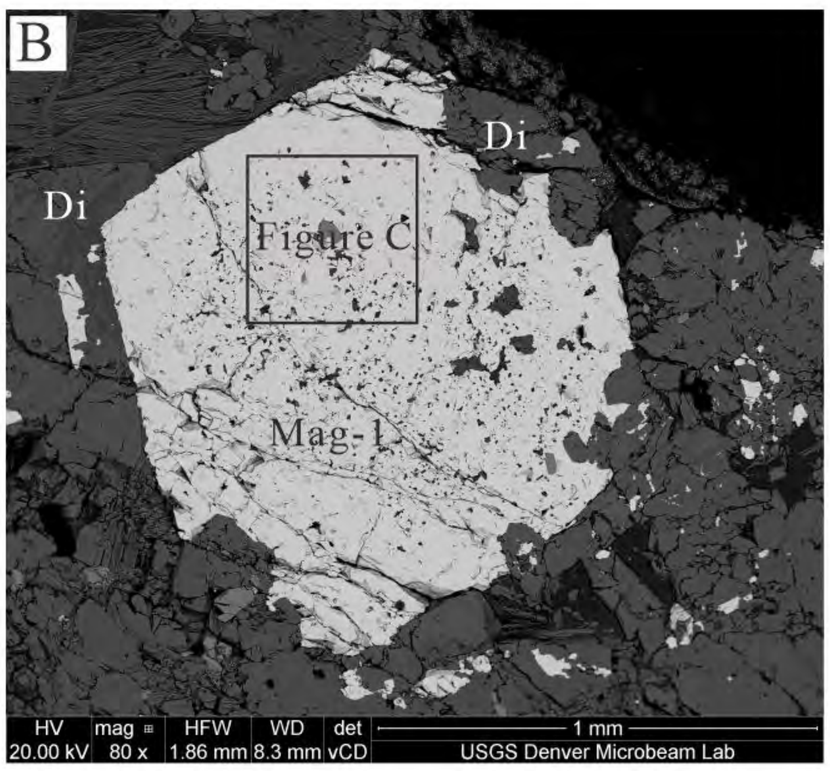
B
Di
Di
Figure C
Mag-1
HV 20.00 kV
mag 80 x
HFW 1.86 mm
WD 8.3 mm
det vCD
1 mm
USGS Denver Microbeam Lab

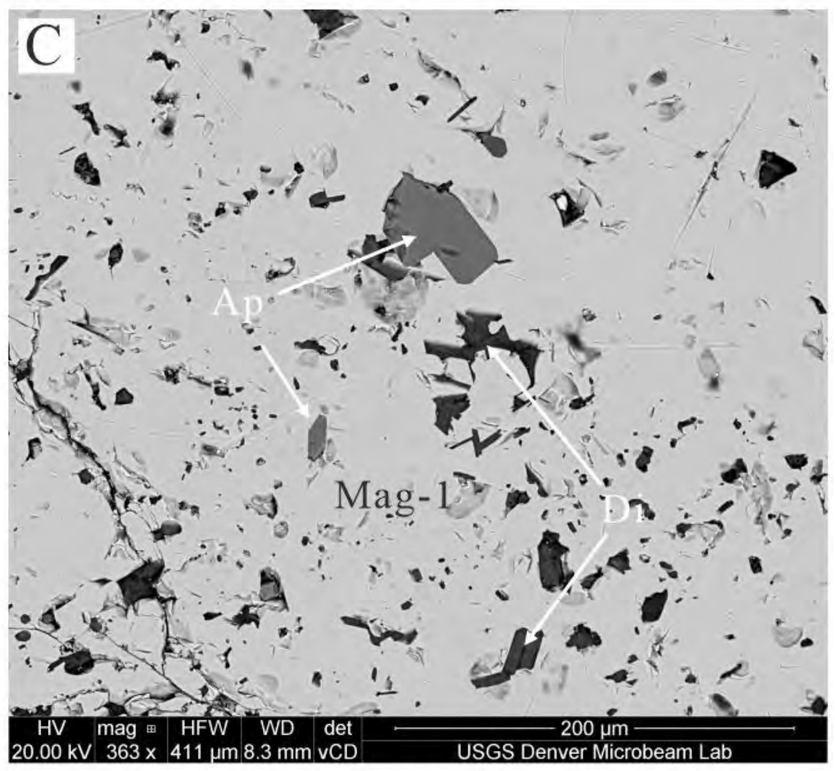
C
Ap
Mag-1
Di
HV 20.00 kV
mag 363 x
HFW 411 µm
WD 8.3 mm
det vCD
200 µm
USGS Denver Microbeam Lab

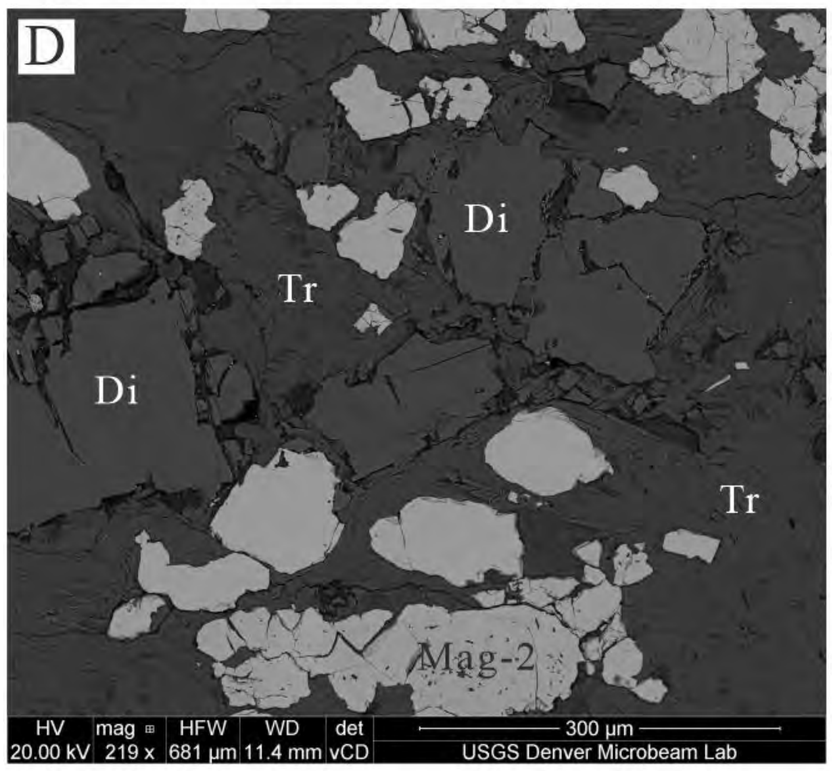
D
Di
Tr
Di
Tr
Mag-2
HV 20.00 kV
mag 219 x
HFW 681 µm
WD 11.4 mm
det vCD
300 µm
USGS Denver Microbeam Lab

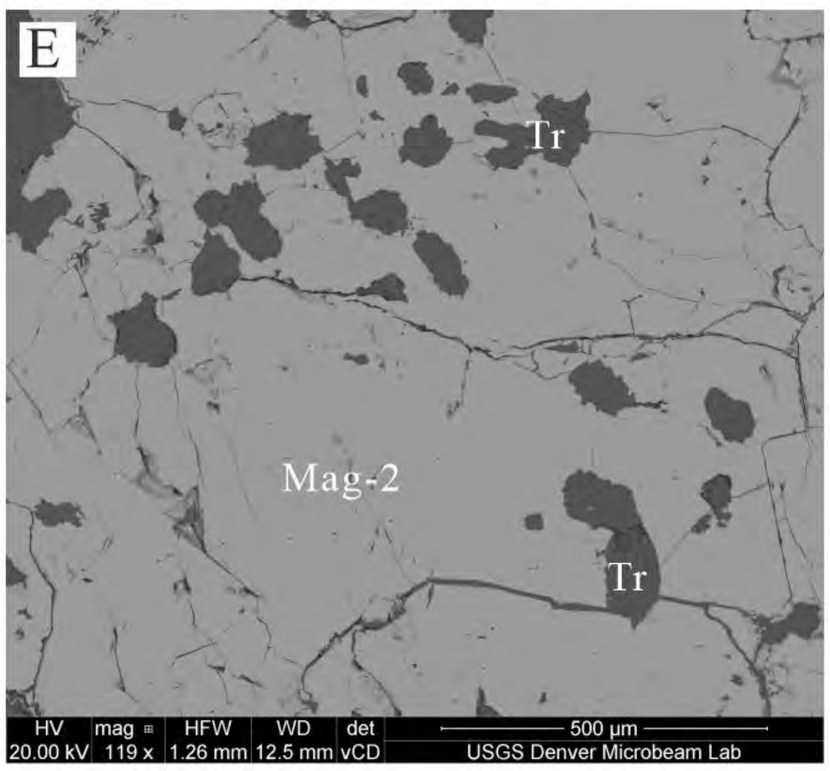
E
Tr
Mag-2
Tr
HV 20.00 kV
mag 119 x
HFW 1.26 mm
WD 12.5 mm
det vCD
500 µm
USGS Denver Microbeam Lab

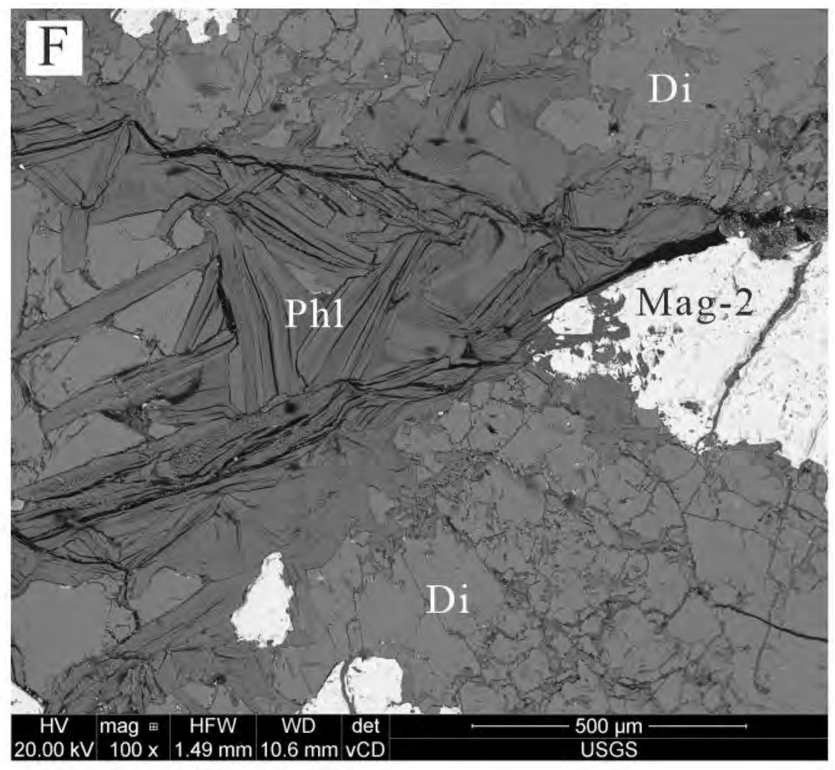
F
Di
Phl
Mag-2
Di
HV 20.00 kV
mag 100 x
HFW 1.49 mm
WD 10.6 mm
det vCD
500 µm
USGS

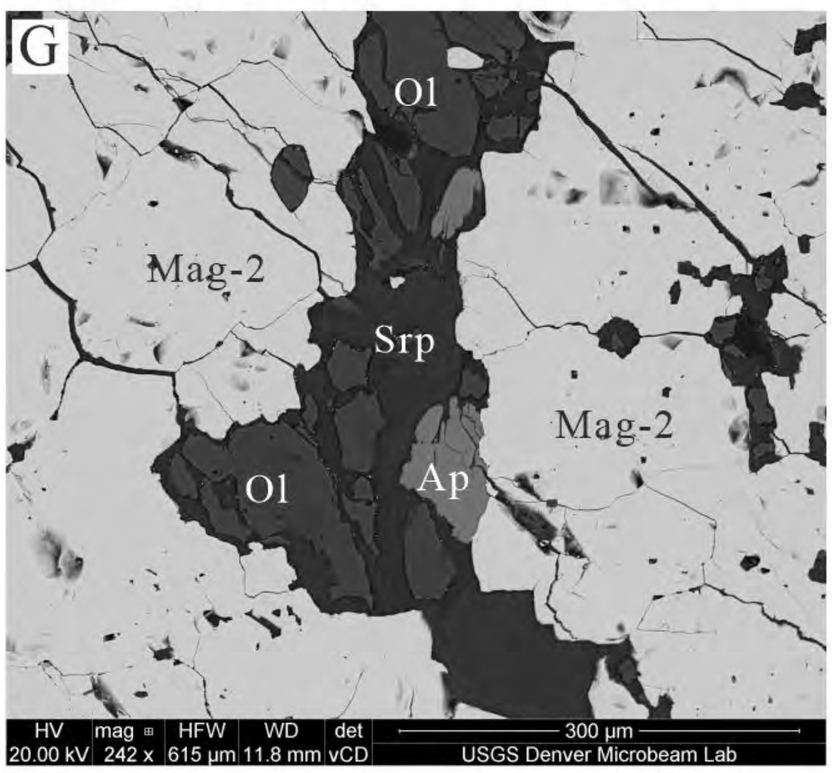
G
Ol
Mag-2
Srp
Mag-2
Ol
Ap
HV 20.00 kV
mag 242 x
HFW 615 µm
WD 11.8 mm
det vCD
300 µm
USGS Denver Microbeam Lab

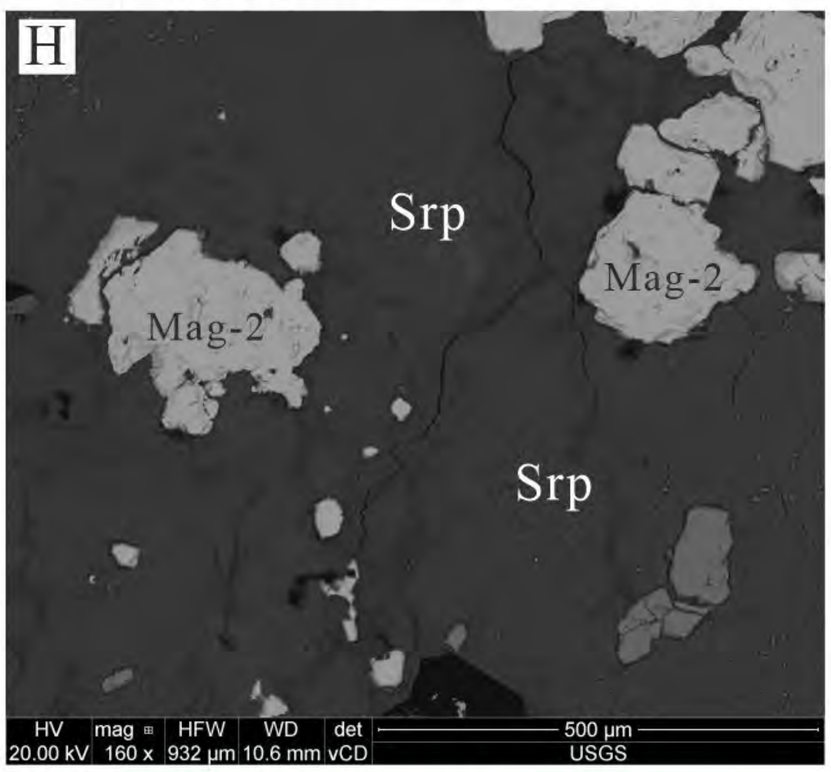
H
Srp
Mag-2
Mag-2
Srp
HV 20.00 kV
mag 160 x
HFW 932 µm
WD 10.6 mm
det vCD
500 µm
USGS

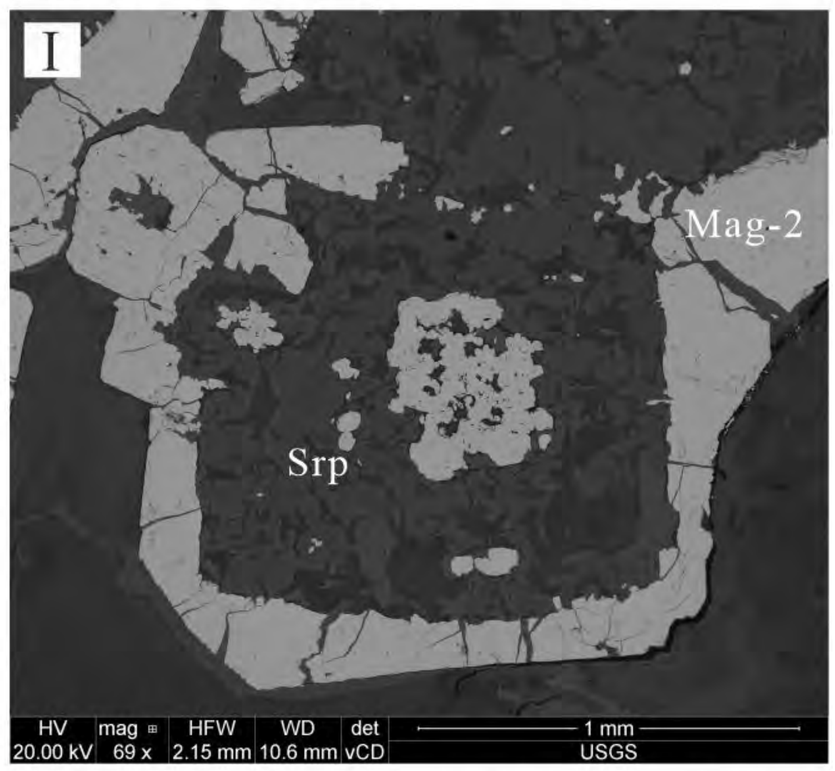
I
Mag-2
Srp
HV 20.00 kV
mag 69 x
HFW 2.15 mm
WD 10.6 mm
det vCD
1 mm
USGS

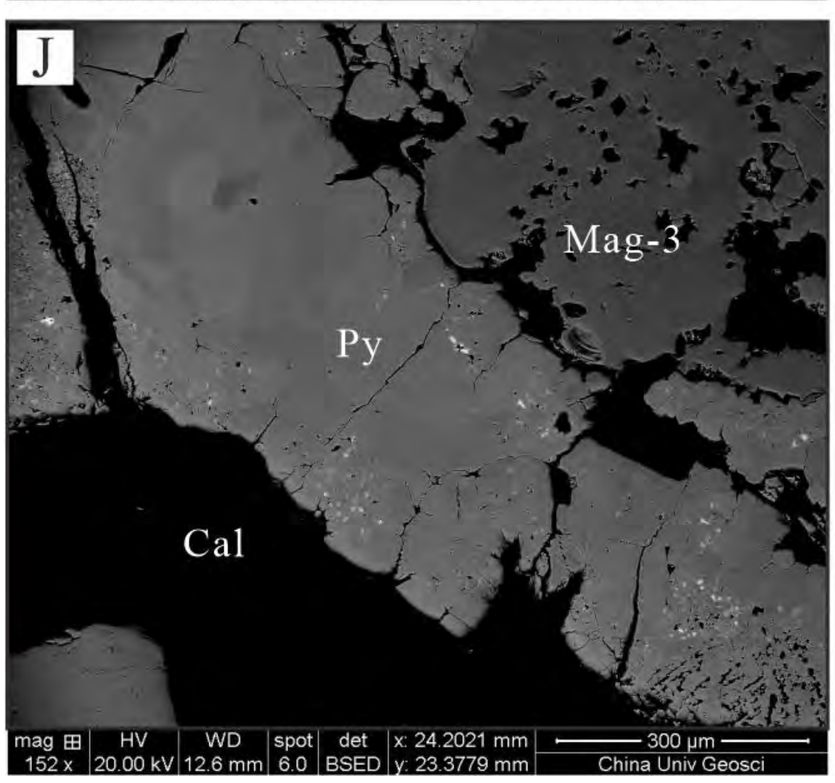
J
Mag-3
Py
Cal
mag 152 x
HV 20.00 kV
WD 12.6 mm
spot 6.0
det BSED
x: 24.2021 mm
y: 23.3779 mm
300 µm
China Univ Geosci

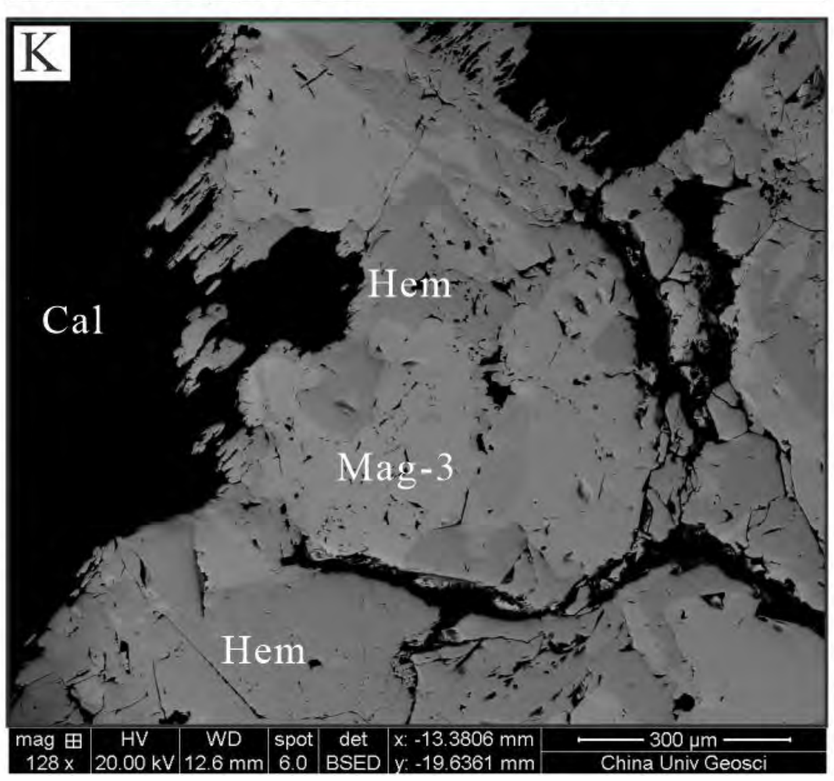
K
Cal
Hem
Mag-3
Hem
mag 128 x
HV 20.00 kV
WD 12.6 mm
spot 6.0
det BSED
x: -13.3806 mm
y: -19.6361 mm
300 µm
China Univ Geosci

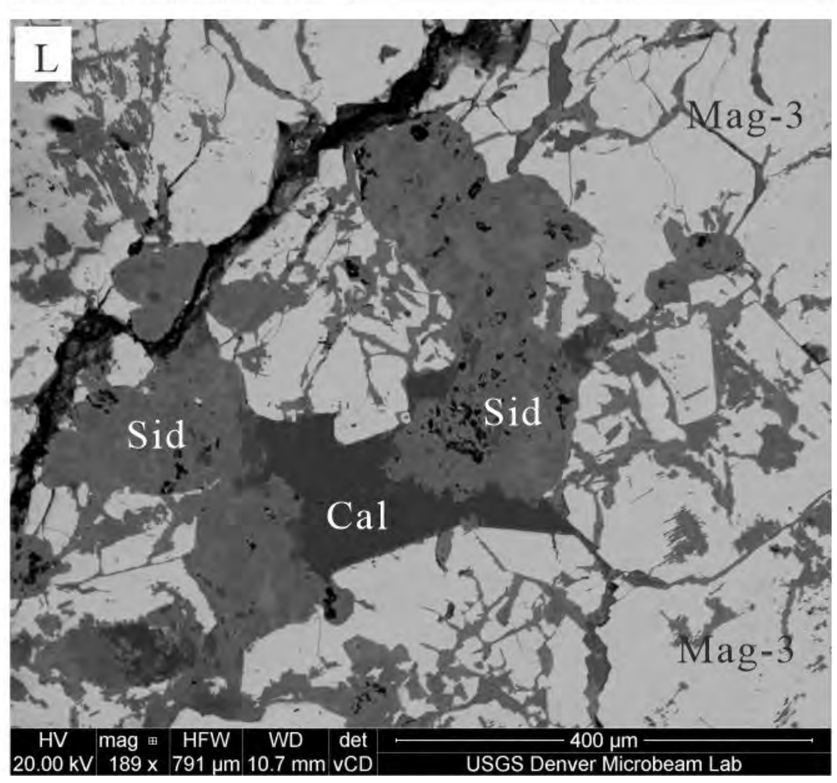
L
Mag-3
Sid
Sid
Cal
Mag-3
HV 20.00 kV
mag 189 x
HFW 791 µm
WD 10.7 mm
det vCD
400 µm
USGS Denver Microbeam Lab

Figure 5

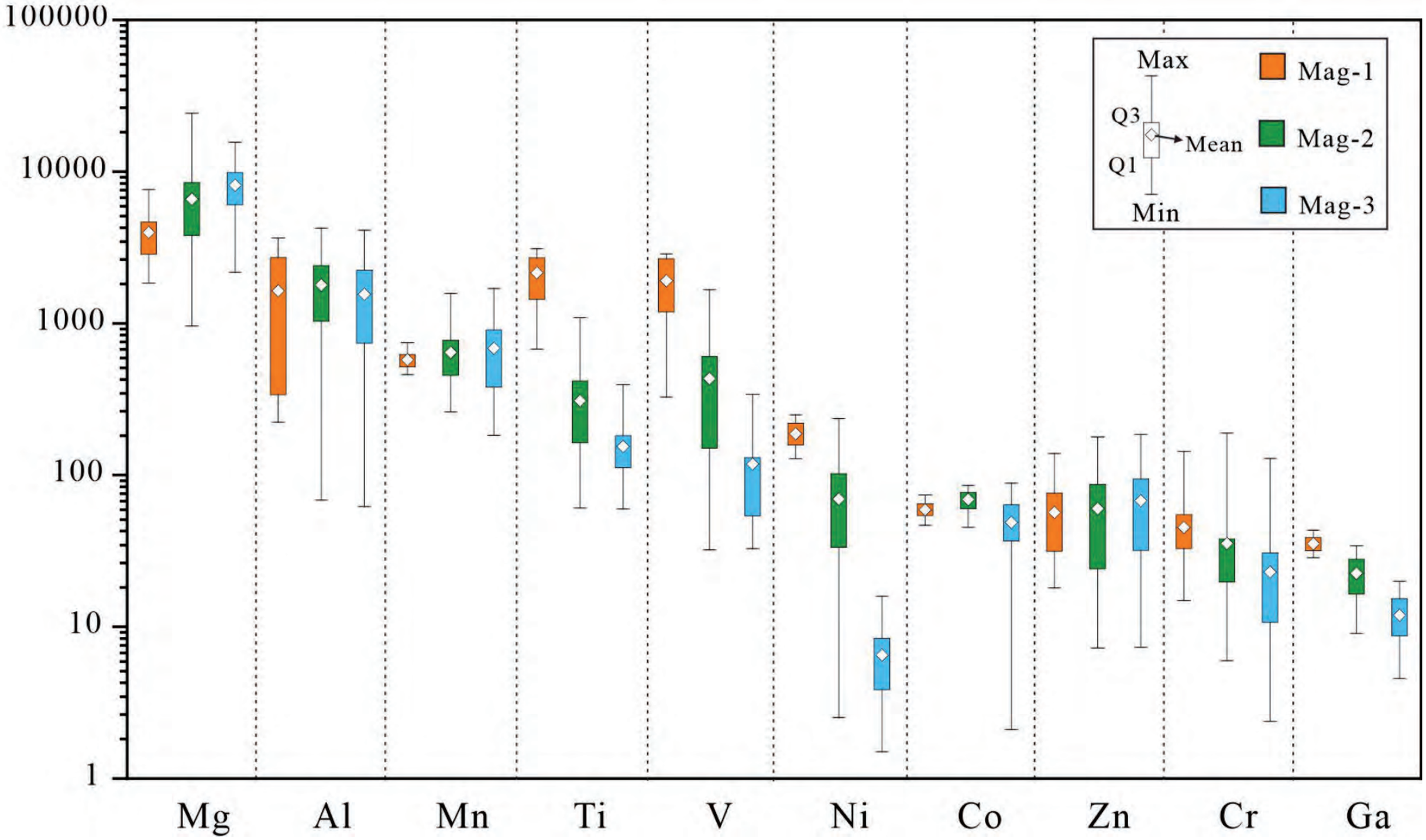
100000
10000
1000
100
10
1
Max
Q3
Mean
Q1
Min
Mag-1
Mag-2
Mag-3
Mg
Al
Mn
Ti
V
Ni
Co
Zn
Cr
Ga

Figure 6

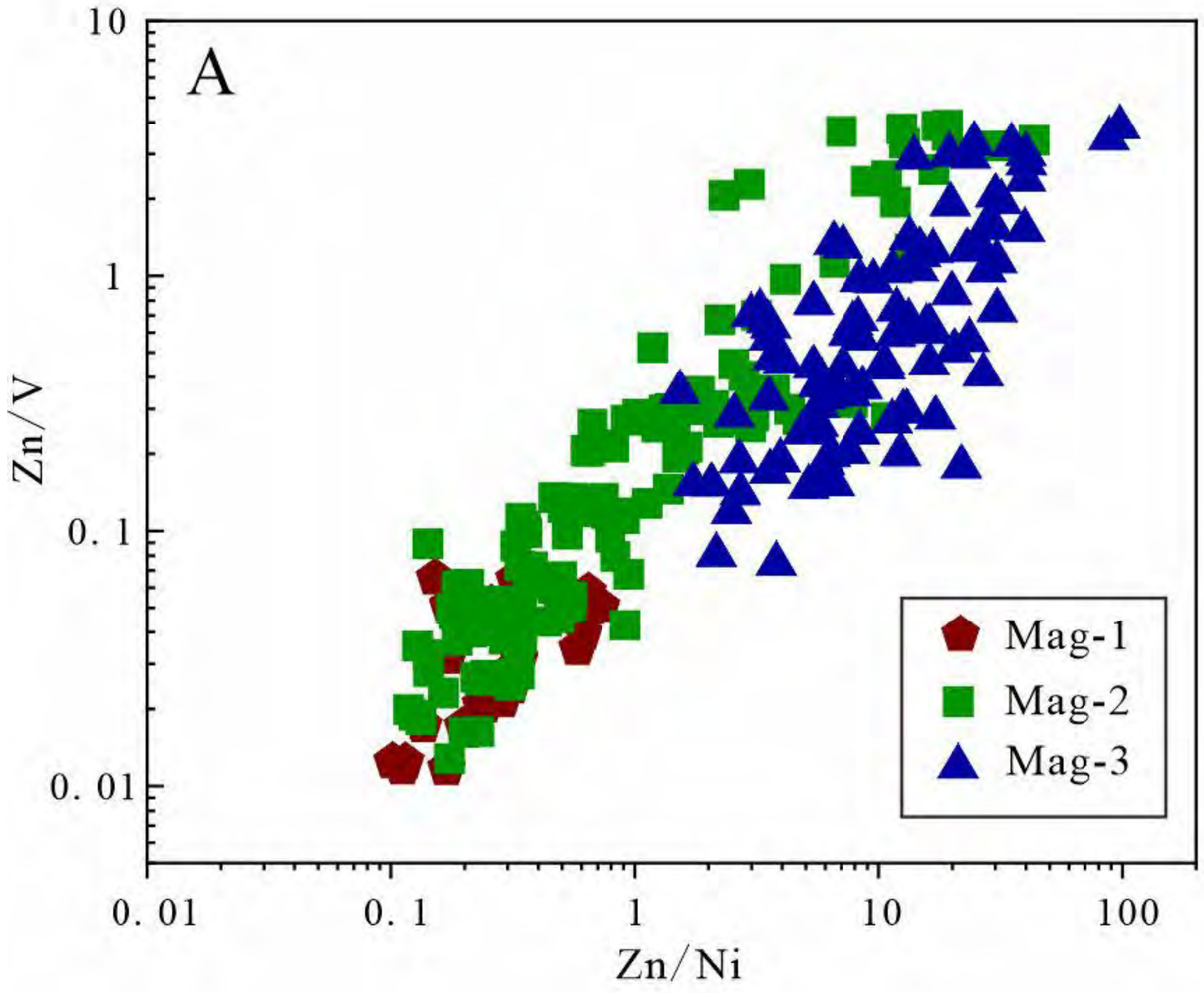
A
Zn/V
Zn/Ni
Mag-1
Mag-2
Mag-3
10
1
0. 1
0. 01
0. 01
0. 1
1
10
100

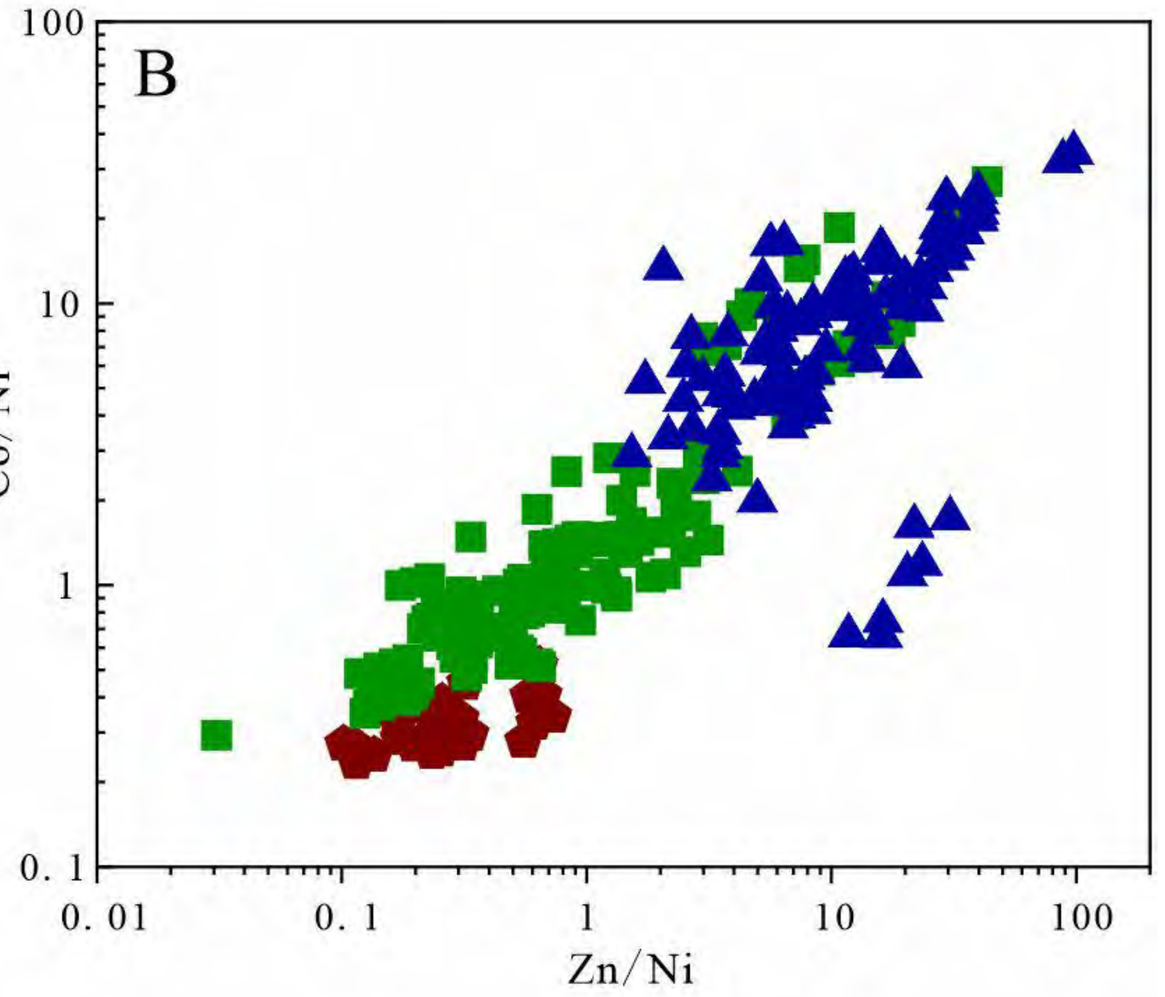
B
Co/Ni
Zn/Ni
100
10
1
0. 1
0. 01
0. 1
1
10
100

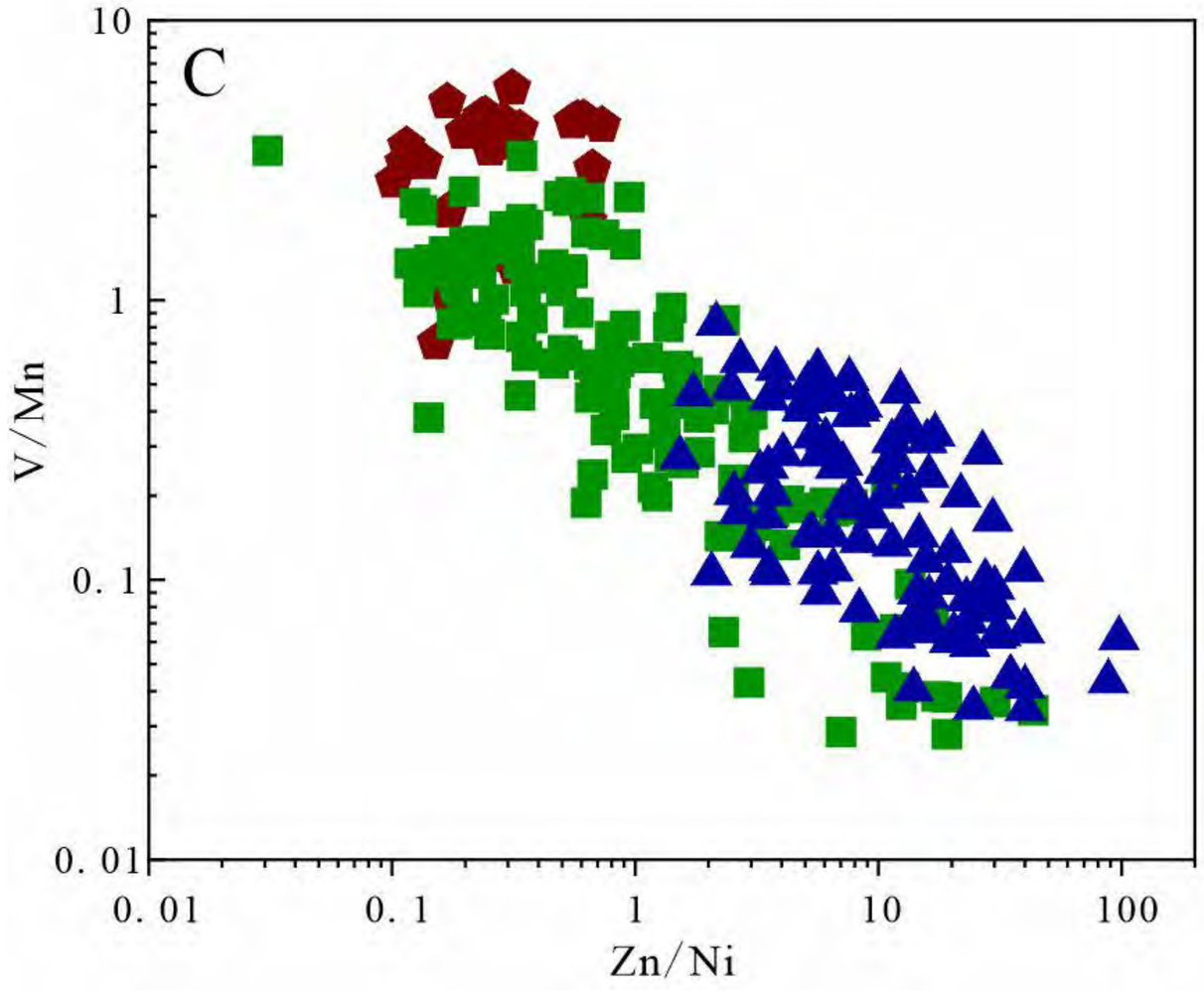
C
V/Mn
Zn/Ni
10
1
0. 1
0. 01
0. 01
0. 1
1
10
100

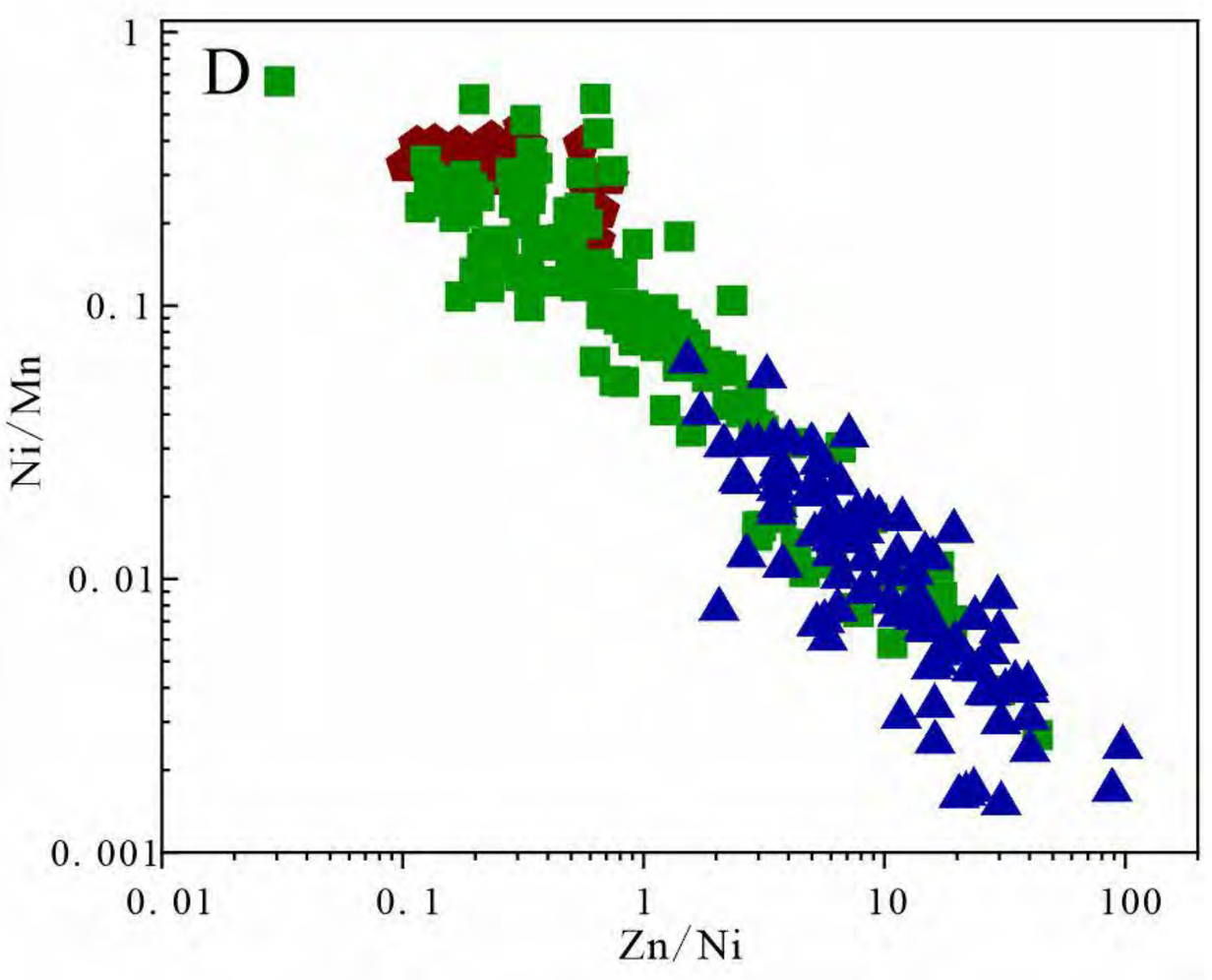
D
Ni/Mn
Zn/Ni
1
0. 1
0. 01
0. 001
0. 01
0. 1
1
10
100

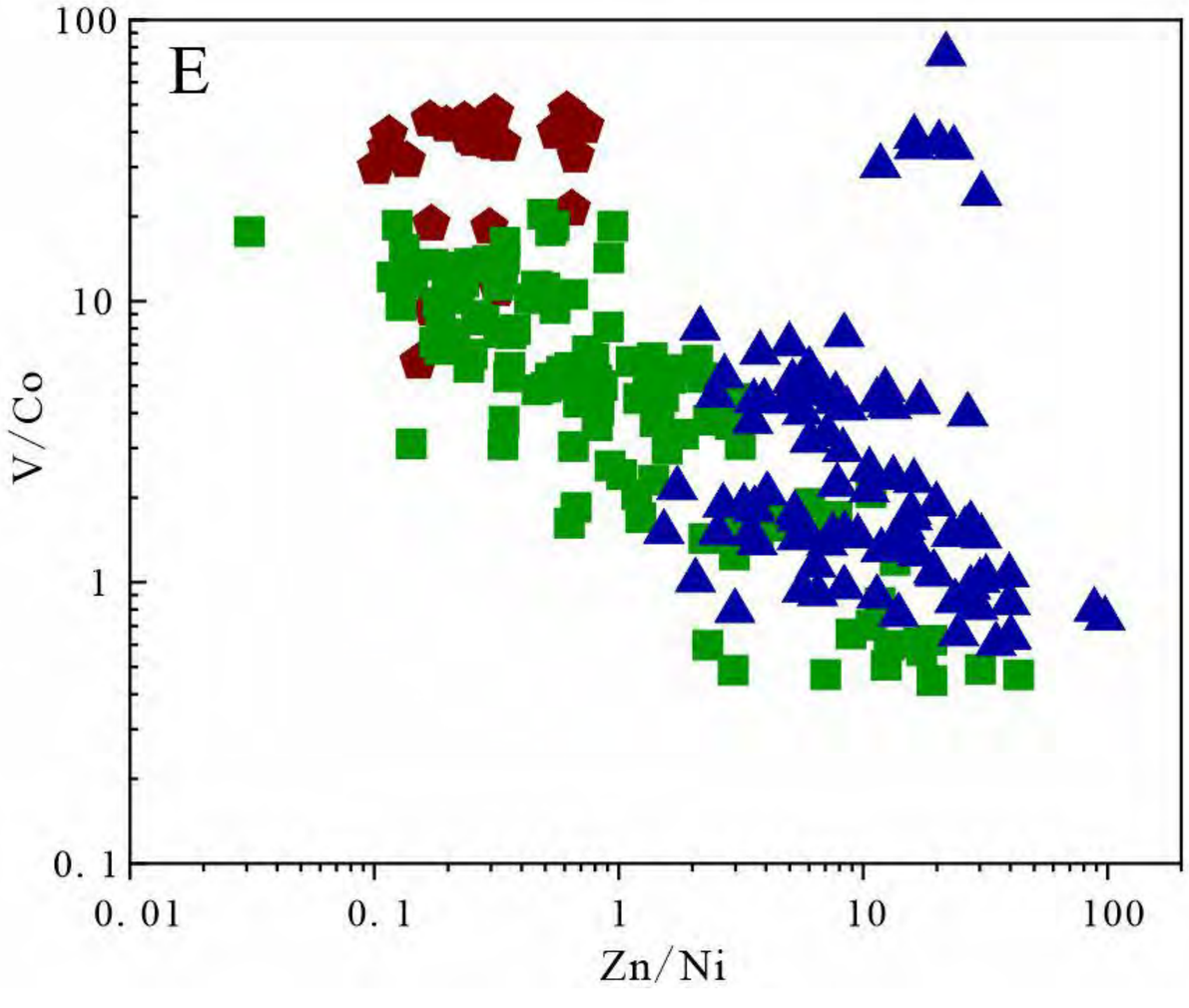
E
V/Co
Zn/Ni
100
10
1
0. 1
0. 01
0. 1
1
10
100

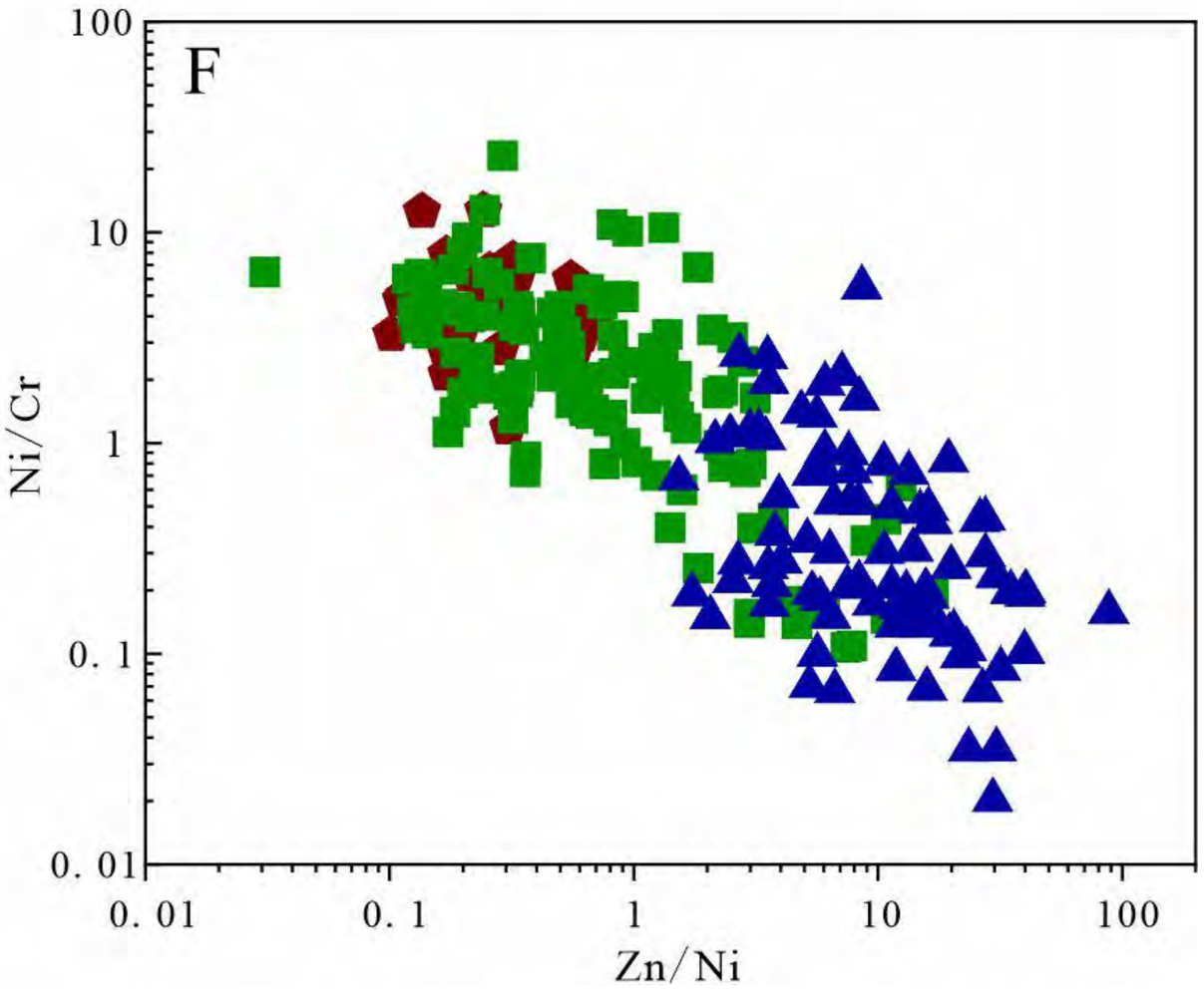
F
Ni/Cr
Zn/Ni
100
10
1
0. 1
0. 01
0. 01
0. 1
1
10
100

Figure 7

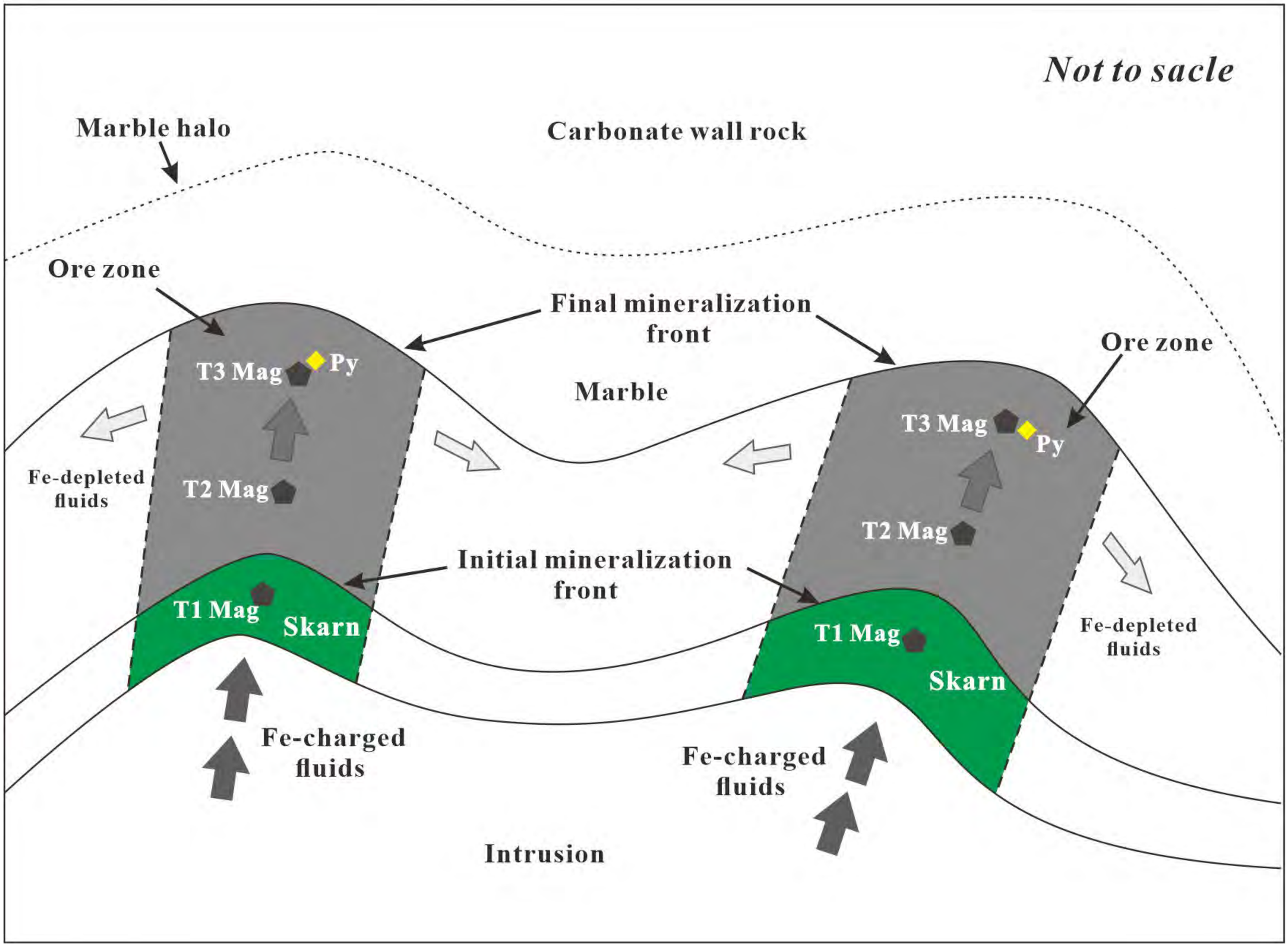
Not to sacle
Marble halo
Carbonate wall rock
Ore zone
Final mineralization front
Ore zone
T3 Mag
Py
Marble
T3 Mag
Py
Fe-depleted fluids
T2 Mag
T2 Mag
Initial mineralization front
T1 Mag
Skarn
T1 Mag
Skarn
Fe-depleted fluids
Fe-charged fluids
Fe-charged fluids
Intrusion

Figure 8

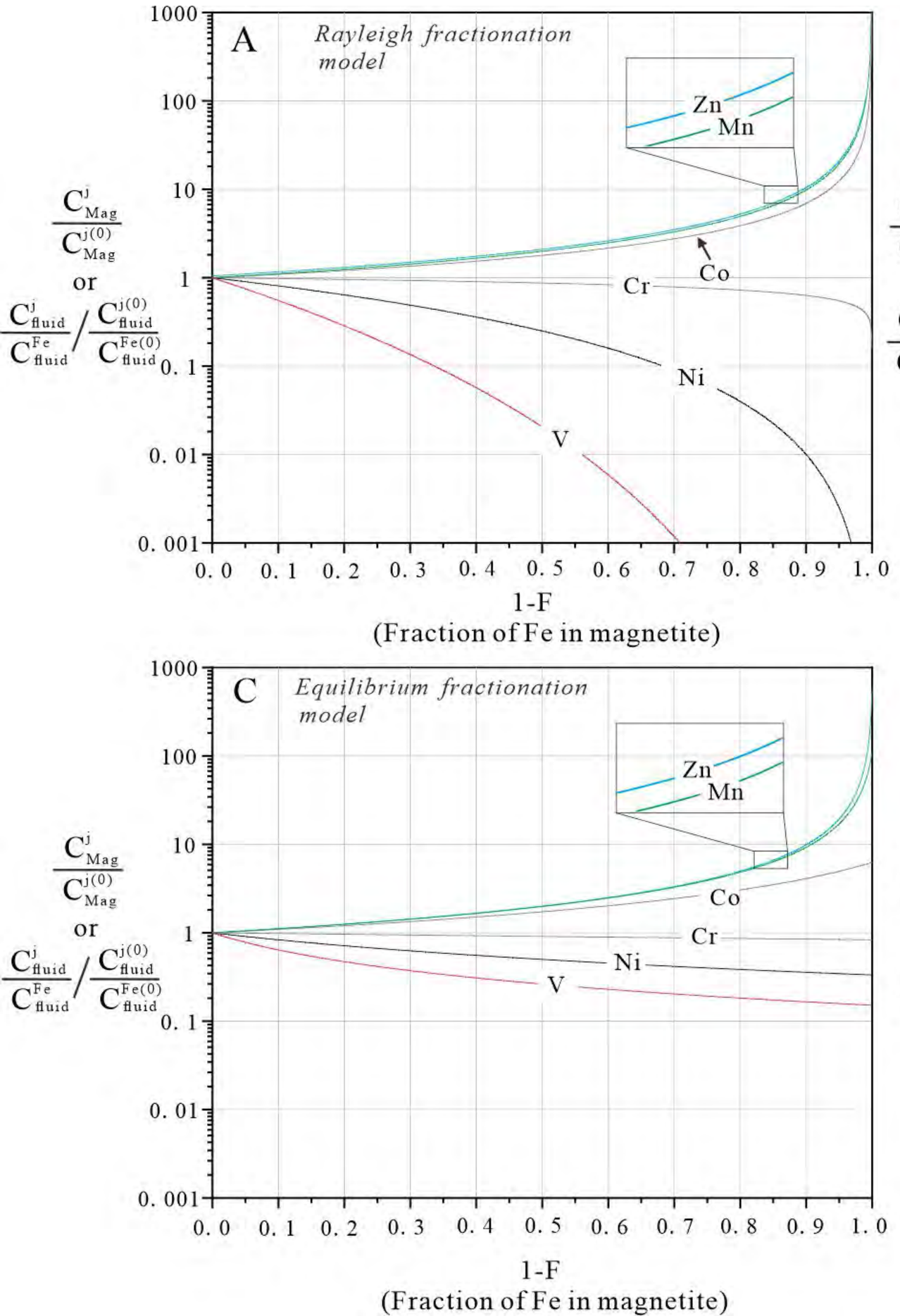
A
Rayleigh fractionation model
Zn
Mn
Co
Cr
Ni
V
1000
100
10
1
0. 1
0. 01
0. 001
0. 0 0. 1 0. 2 0. 3 0. 4 0. 5 0. 6 0. 7 0. 8 0. 9 1. 0
1-F
(Fraction of Fe in magnetite)
$\frac{C^{j}_{Mag}}{C^{j(0)}_{Mag}}$ or $\frac{C^{j}_{fluid}}{C^{Fe}_{fluid}} / \frac{C^{j(0)}_{fluid}}{C^{Fe(0)}_{fluid}}$

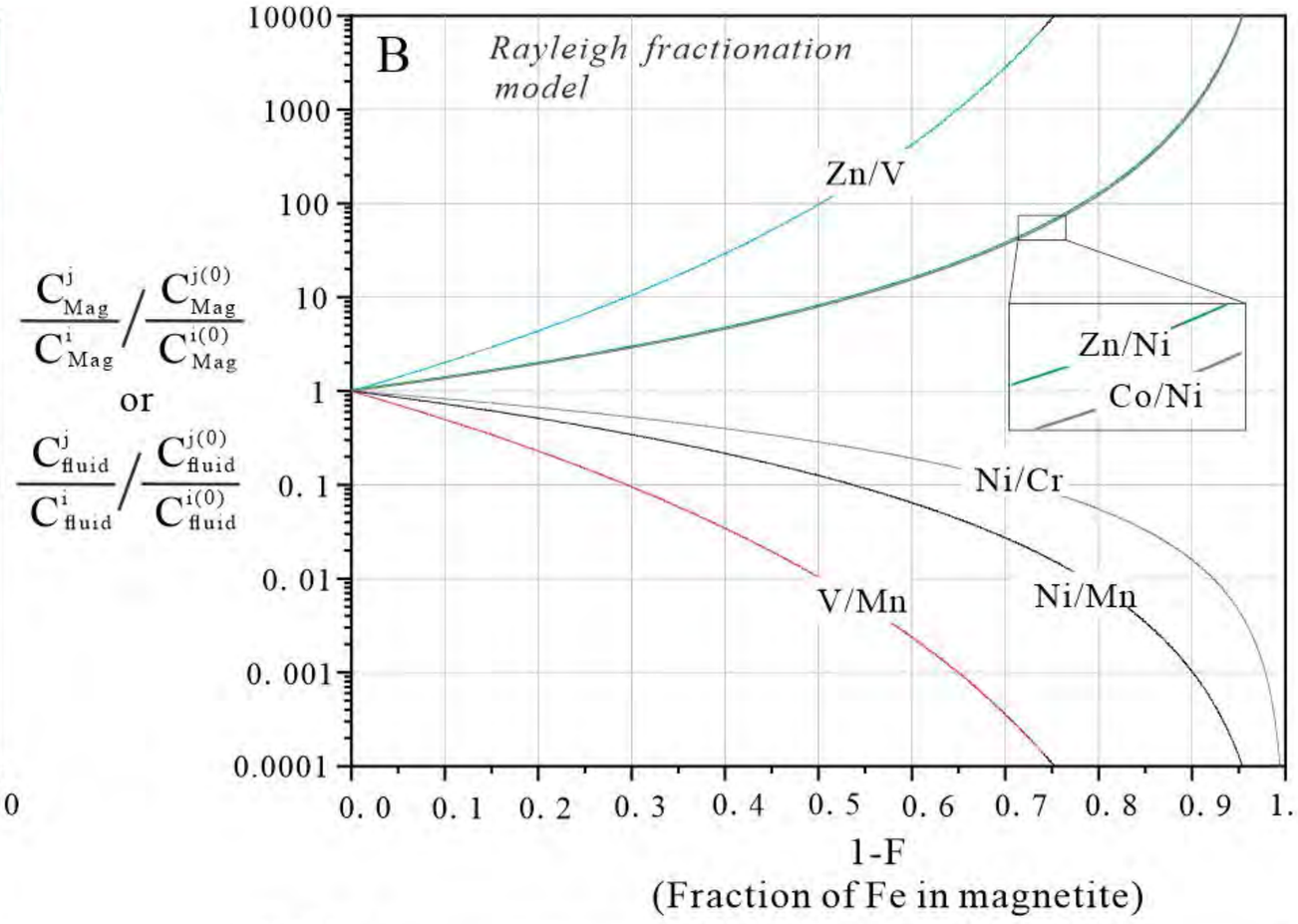
B
Rayleigh fractionation model
Zn/V
Zn/Ni
Co/Ni
Ni/Cr
Ni/Mn
V/Mn
10000
1000
100
10
1
0. 1
0. 01
0. 001
0.0001
0. 0 0. 1 0. 2 0. 3 0. 4 0. 5 0. 6 0. 7 0. 8 0. 9 1. 0
1-F
(Fraction of Fe in magnetite)
$\frac{C^{j}_{Mag}}{C^{i}_{Mag}} / \frac{C^{j(0)}_{Mag}}{C^{i(0)}_{Mag}}$ or $\frac{C^{j}_{fluid}}{C^{i}_{fluid}} / \frac{C^{j(0)}_{fluid}}{C^{i(0)}_{fluid}}$

C
Equilibrium fractionation model
Zn
Mn
Co
Cr
Ni
V
1000
100
10
1
0. 1
0. 01
0. 001
0. 0 0. 1 0. 2 0. 3 0. 4 0. 5 0. 6 0. 7 0. 8 0. 9 1. 0
1-F
(Fraction of Fe in magnetite)
$\frac{C^{j}_{Mag}}{C^{j(0)}_{Mag}}$ or $\frac{C^{j}_{fluid}}{C^{Fe}_{fluid}} / \frac{C^{j(0)}_{fluid}}{C^{Fe(0)}_{fluid}}$

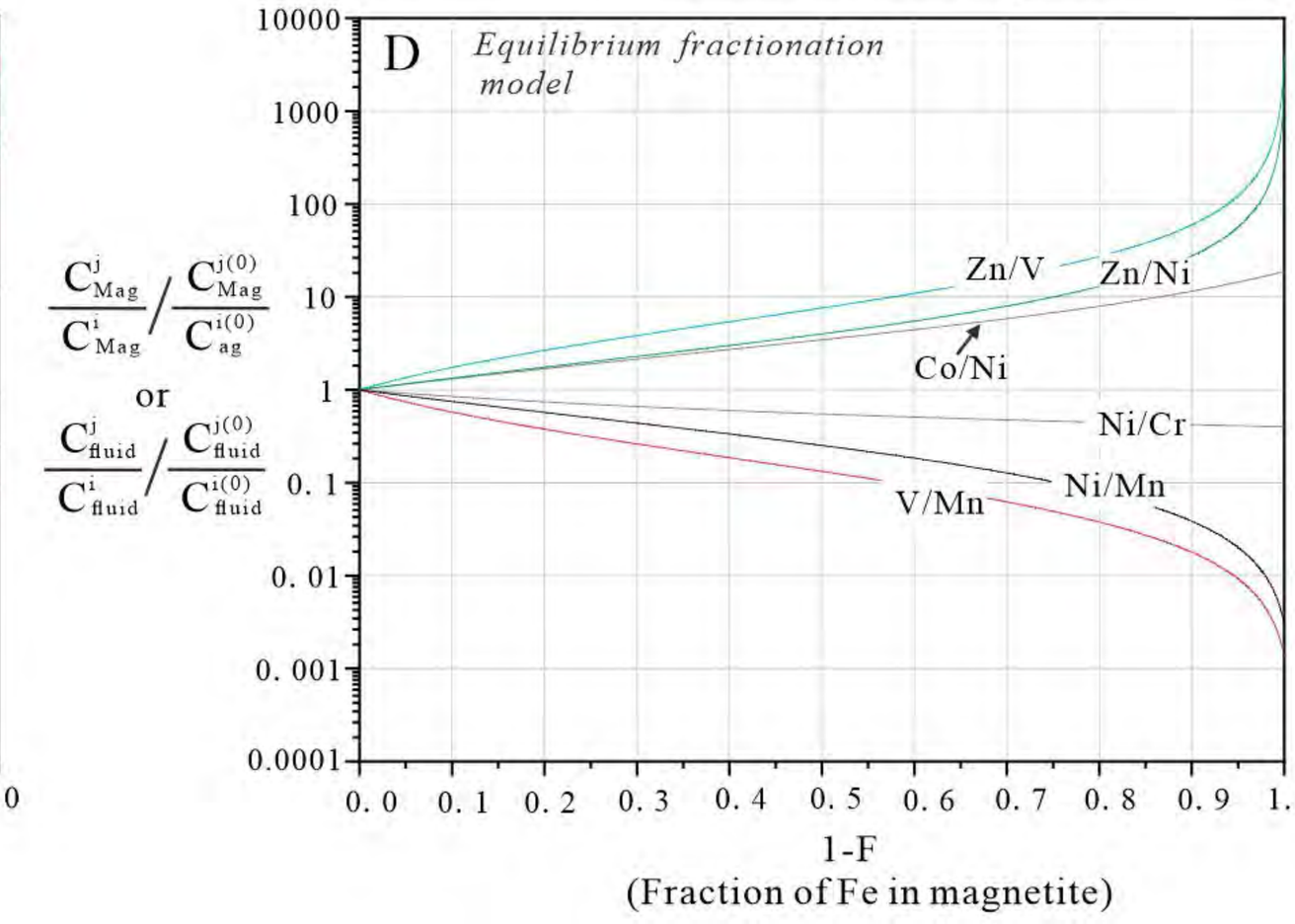
D
Equilibrium fractionation model
Zn/V
Zn/Ni
Co/Ni
Ni/Cr
Ni/Mn
V/Mn
10000
1000
100
10
1
0. 1
0. 01
0. 001
0.0001
0. 0 0. 1 0. 2 0. 3 0. 4 0. 5 0. 6 0. 7 0. 8 0. 9 1. 0
1-F
(Fraction of Fe in magnetite)
$\frac{C^{j}_{Mag}}{C^{i}_{Mag}} / \frac{C^{j(0)}_{Mag}}{C^{i(0)}_{ag}}$ or $\frac{C^{j}_{fluid}}{C^{i}_{fluid}} / \frac{C^{j(0)}_{fluid}}{C^{i(0)}_{fluid}}$

Figure 9

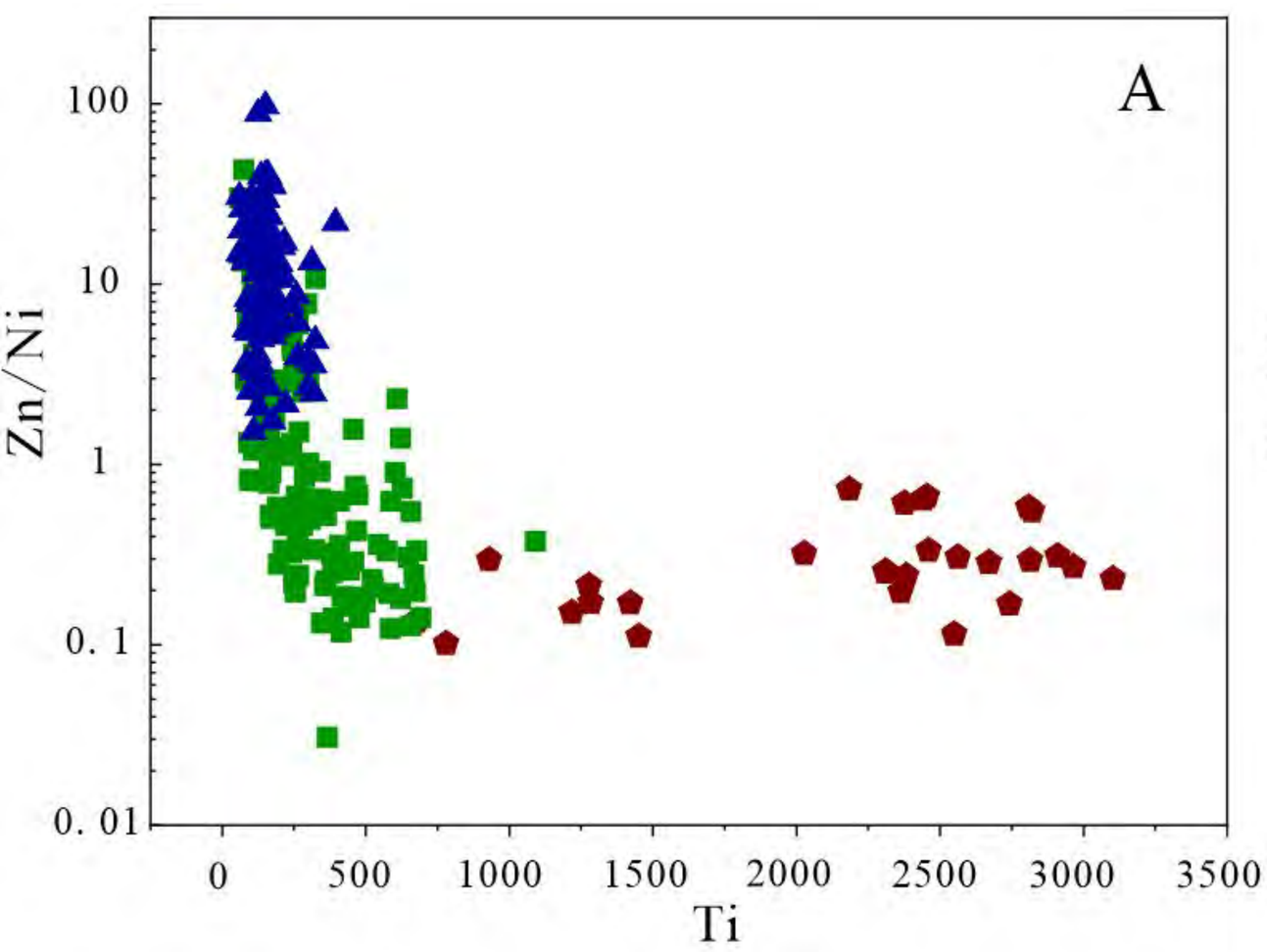
A
100
10
1
0. 1
0. 01
Zn/Ni
0
500
1000
1500
2000
2500
3000
3500
Ti

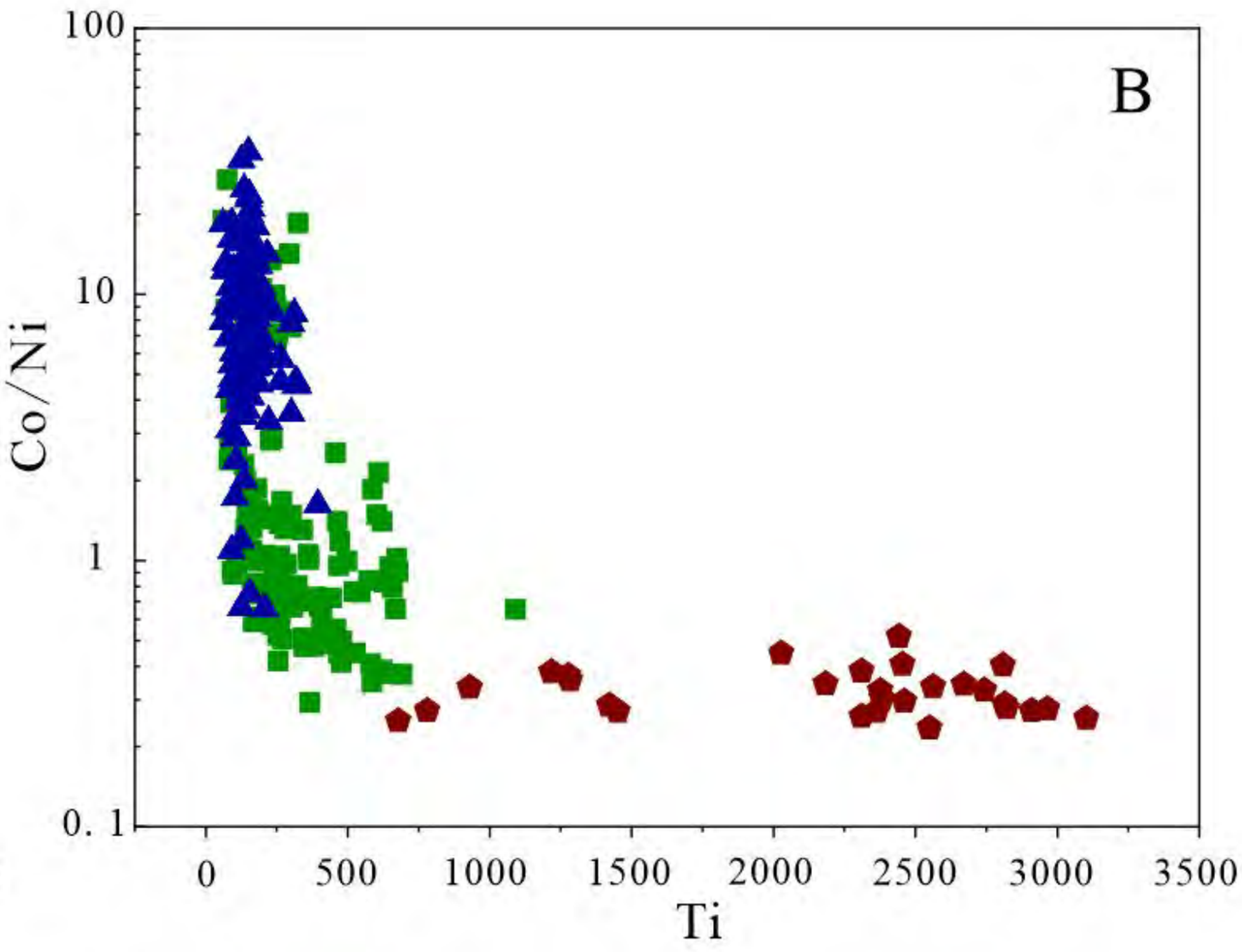
B
100
10
1
0. 1
Co/Ni
0
500
1000
1500
2000
2500
3000
3500
Ti

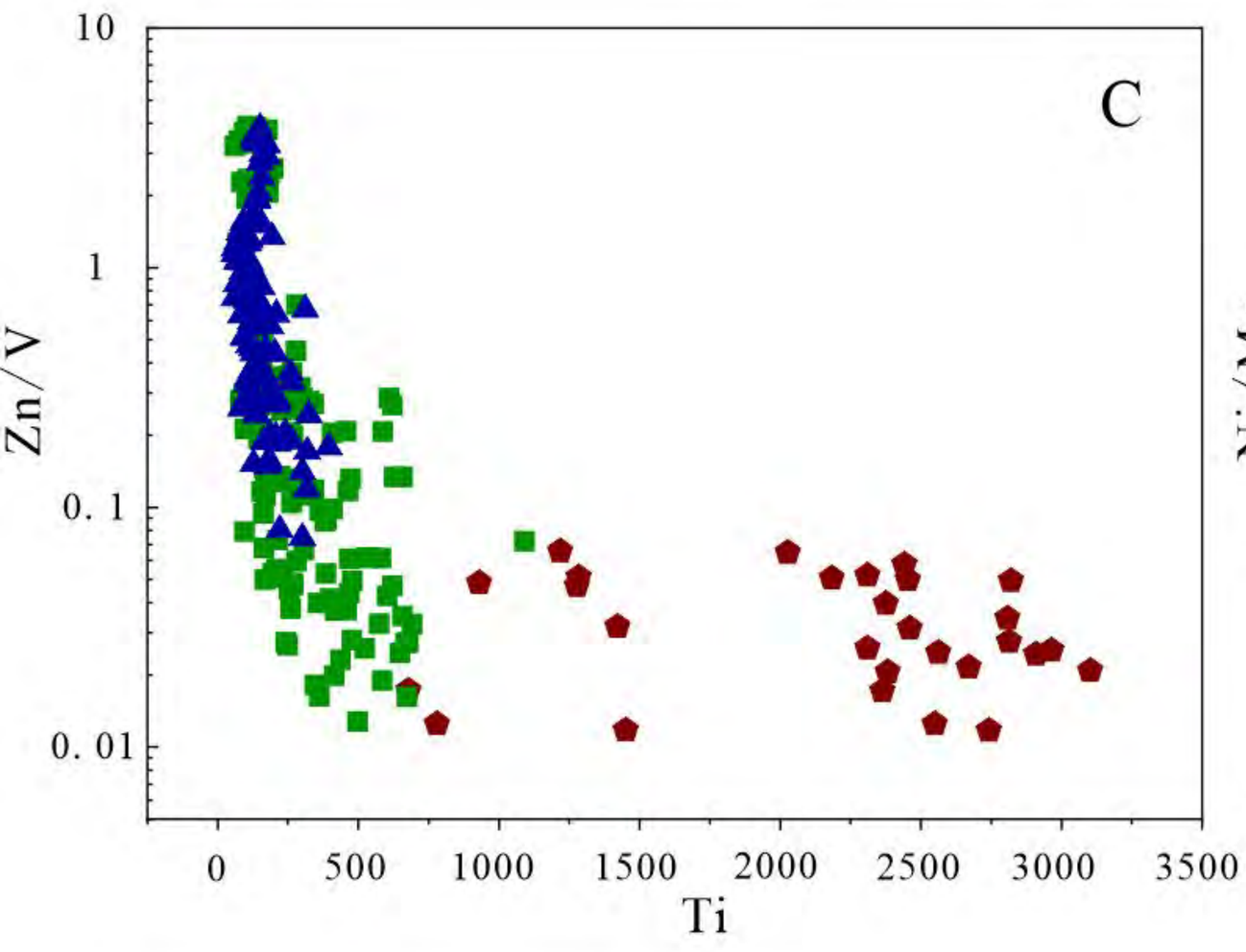
C
10
1
0. 1
0. 01
Zn/V
0
500
1000
1500
2000
2500
3000
3500
Ti

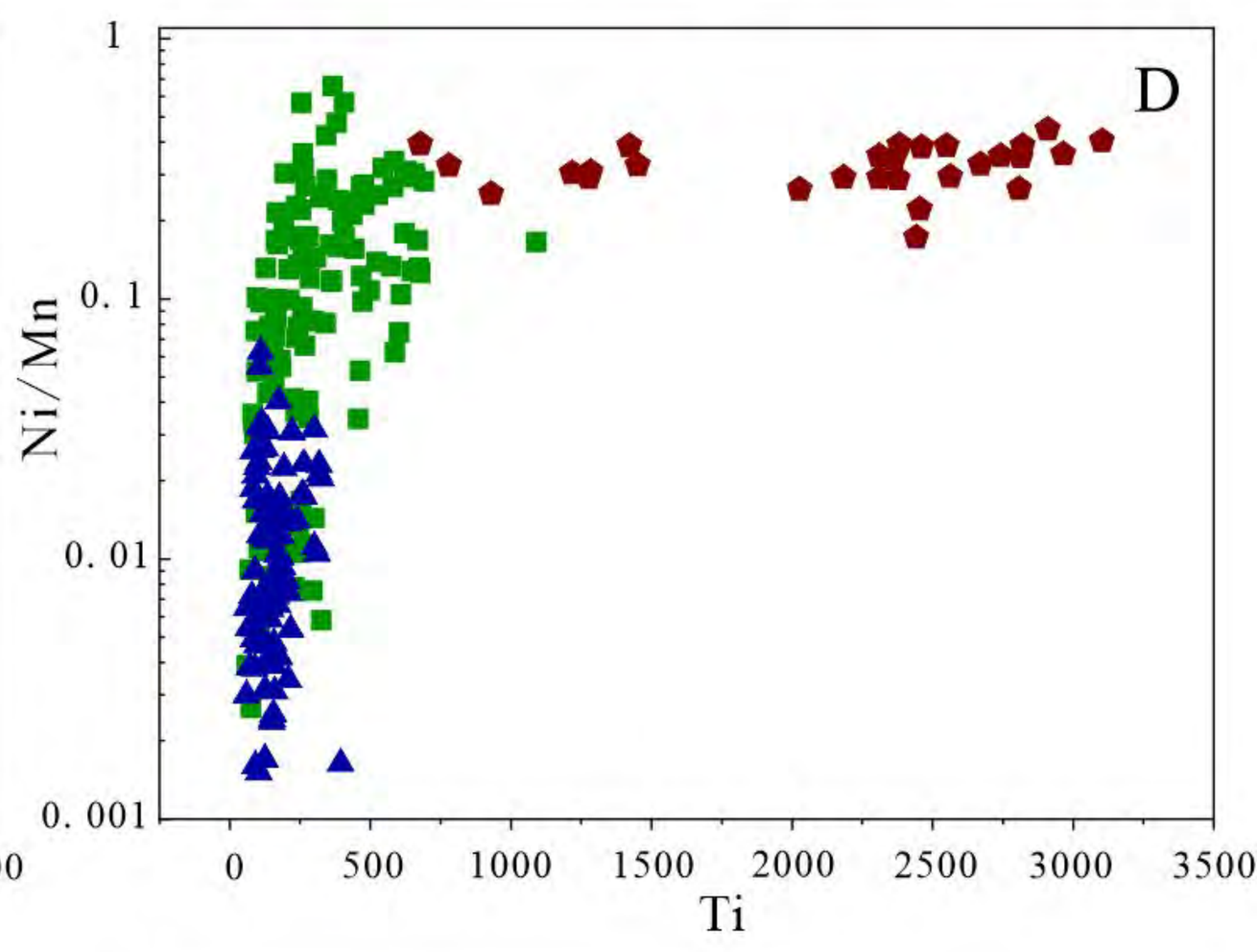
D
1
0. 1
0. 01
0. 001
Ni/Mn
0
500
1000
1500
2000
2500
3000
3500
Ti

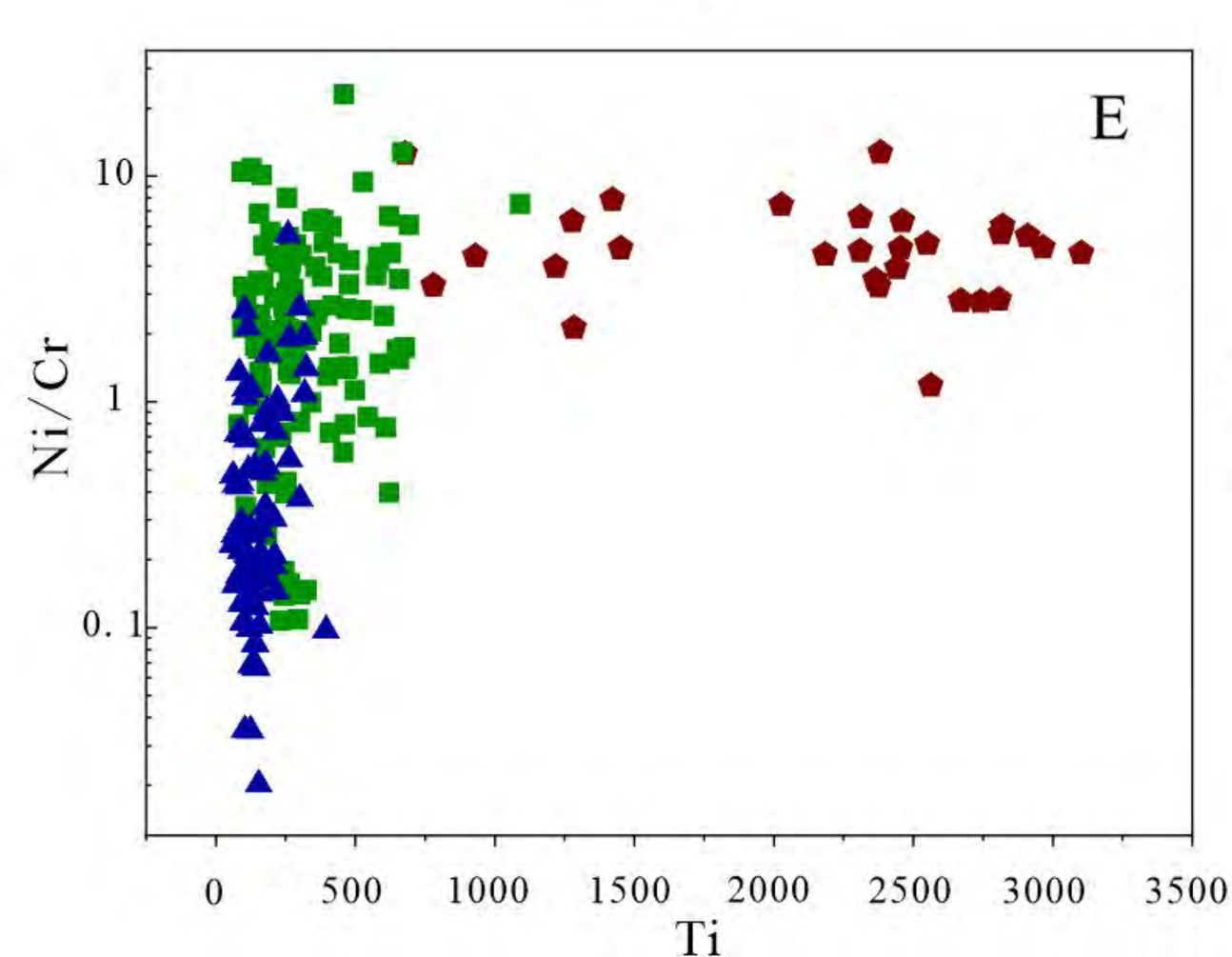
E
10
1
0. 1
Ni/Cr
0
500
1000
1500
2000
2500
3000
3500
Ti

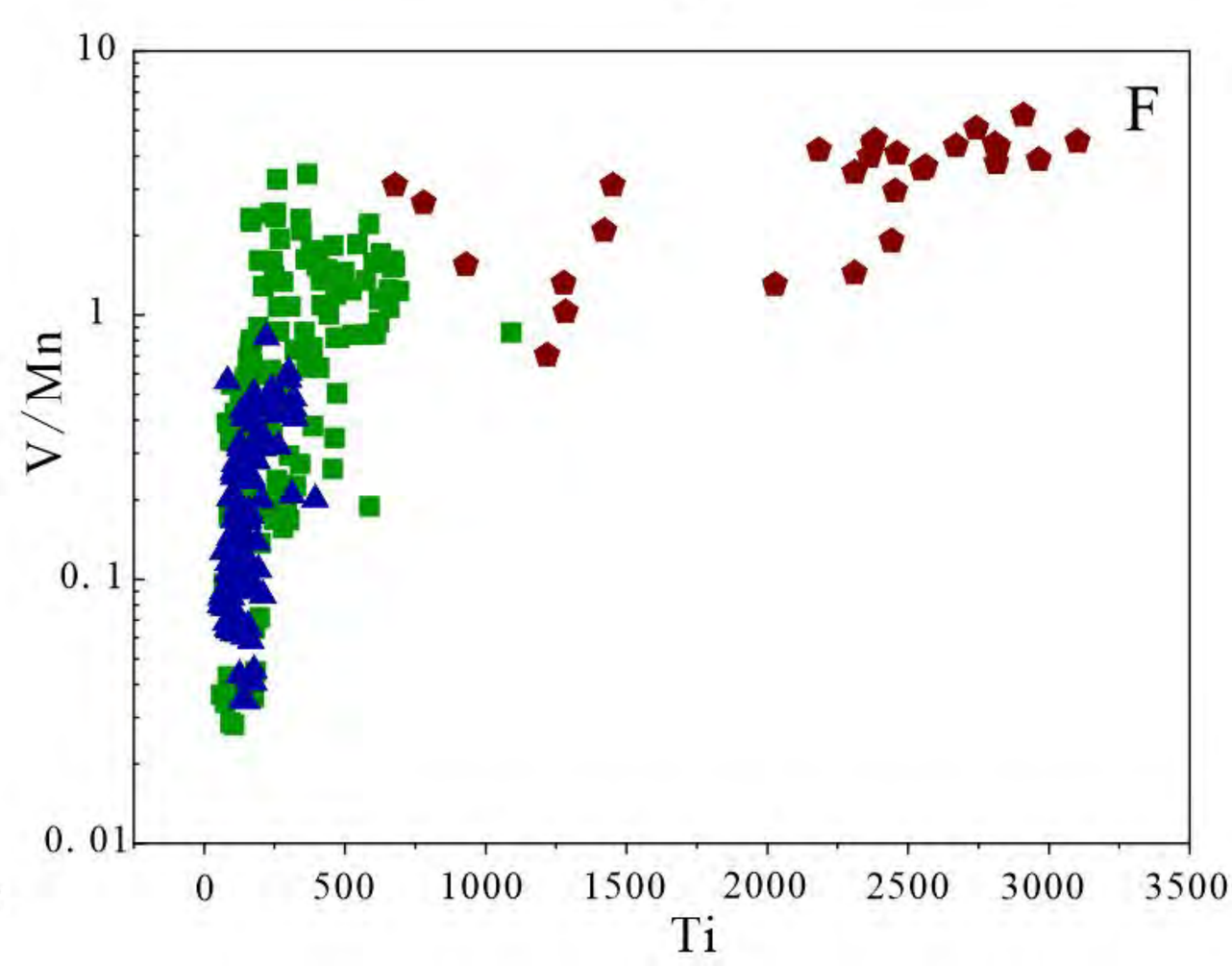
F
10
1
0. 1
0. 01
V/Mn
0
500
1000
1500
2000
2500
3000
3500
Ti